Slender phoretic theory of chemically active filaments

Panayiota Katsamba[1], **Sébastien Michelin**[2]
and Thomas D. Montenegro-Johnson[1,†]

[1]School of Mathematics, University of Birmingham, Edgbaston, Birmingham B15 2TT, UK

[2]LadHyX – Département de Mécanique, CNRS – Ecole Polytechnique, Institut Polytechnique de Paris, 91128 Palaiseau, France

Artificial microswimmers, or 'microbots', have the potential to revolutionise non-invasive medicine and microfluidics. Microbots that are powered by self-phoretic mechanisms, such as Janus particles, often harness a solute fuel in their environment. Traditionally, self-phoretic particles are point like, but slender phoretic rods have become an increasingly prevalent design. While there has been substantial interest in creating efficient asymptotic theories for slender phoretic rods, hitherto such theories have been restricted to straight rods with axisymmetric patterning. However, modern manufacturing methods will soon allow fabrication of slender phoretic filaments with complex three-dimensional shapes. In this paper, we develop a slender body theory for the solute of self-diffusiophoretic filaments of arbitrary three-dimensional shape and patterning. We demonstrate analytically that, unlike other slender body theories, first-order azimuthal variations arising from curvature and confinement can make a leading-order contribution to the swimming kinematics.

---

1. Introduction

Artificial microscale swimmers (microbots) are a novel technology with promising applications in medicine (Nelson, Kaliakatsos & Abbott 2010) and microfluidics (Maggi *et al.* 2016). Microbots can be broadly classified by whether their propulsion is externally actuated, or fuel based. Externally actuated microbots are typically magnetised and actuated by a periodic magnetic field, for example rigid helical filaments attached to a magnetised head (Ghosh & Fischer 2009; Zhang *et al.* 2009*a*,*b*; Gao *et al.* 2010), and 'sperm-like' microbots, that move a flexible tail (Dreyfus *et al.* 2005). Other externally actuated microbots are powered by bubbles driven to oscillate via applied ultrasound (Bertin *et al.* 2015). In contrast, fuel-based microbots harvest fuel from their surroundings to self-propel (Paxton *et al.* 2004; Williams *et al.* 2014). One class of such fuel-based microbots are self-diffusiophoretic (autophoretic) particles. In autophoresis, surface patterning of a particle with a catalyst gives rise to

† Email address for correspondence: t.d.johnson@bham.ac.uk

differential surface reaction, allowing the particle to self-generate solute concentration gradients which drive a propulsive slip flow (Paxton *et al.* 2004).

Typically, autophoretic particles are spheroids, disks, rods and, recently, tori (Baker *et al.* 2019), partially coated in a catalyst. Nature at the microscale is, in contrast, proliferated by flexible active filaments. Such phoretic filaments could exhibit exciting dynamic behaviours, such as spontaneous buckling and periodic oscillations, and even be selectively controlled via targeted shape change. However, dynamic simulations of slender objects can be computationally costly, owing to the need to accurately resolve multiple length scales. As such, there has been a significant drive to develop a slender body theory for autophoretic particles. Such theories not only have the benefit of numerical efficiency, but are also able to provide analytical insight into dynamic behaviours.

The development of slender body theories (SBT) of the dynamics of filaments in viscous fluids represents a *magnum opus* in low Reynolds number research, spanning nearly 70 years. SBT has provided the basis for numerous insights in bioactive flows, for instance cilia-driven symmetry-breaking flow in vertebrates (Smith, Montenegro-Johnson & Lopes 2019), mucociliary clearance (Smith, Gaffney & Blake 2008) and sperm motility (Gaffney *et al.* 2011), amongst others. Indeed, SBT continues to be an invaluable tool for dynamic fluid–filament interaction simulations (Hall-McNair *et al.* 2019; Schoeller *et al.* 2019; Walker *et al.* 2019) where boundary element methods would prove prohibitively costly.

SBT was pioneered by Hancock (1953), who modelled the beating tails of microorganisms via line distributions of Stokes flow singularities, from which resistive force theory was soon after derived (Gray & Hancock 1955). This work was later formalised into a framework of matched-asymptotic expansions (Cox 1970), with the inner problem representing flow past a two-dimensional (2-D) cylinder, and the outer problem a distribution of singularities. Improved, algebraically accurate, SBTs were then developed (e.g. Johnson 1979), often using Chwang and Wu's exact singularity distribution for a prolate spheroid (Chwang & Wu 1975). For a more detailed overview, see Lauga & Powers (2009). More recently, Koens & Lauga (2018) showed that the boundary integral representation of Stokes flow contains SBT, via asymptotic expansion of the integral kernels.

For phoretic particles, Yariv (2008) developed an SBT for the electrophoretic motion of slender straight rods with a varying cross-section. A similar approach was used later by Schnitzer & Yariv (2015) for studying slender self-diffusiophoretic particles with axisymmetric chemical activity, and Ibrahim, Golestanian & Liverpool (2017) used a matched-asymptotic expansion to examine how the end shape and cross-sectional profile of straight slender catalytic rods affect swimming speed. Recently, Yariv (2019) extended the work of Schnitzer & Yariv (2015) to more complex reaction kinetics that depend on the Damköhler number.

In this paper, we extend this previous work to phoretic filaments of arbitrary 3-D centreline, axisymmetric but varying cross-section and arbitrary chemical patterning, by exploiting a matched-asymptotic expansion from a boundary integral representation of Laplace's equation, as developed by Koens & Lauga (2018) for slender bodies in viscous flow. For axisymmetric particles, azimuthal variations in concentration, which are sub-leading order, have a leading-order effect on the particle kinematics when the particle centreline is curved. As such, our slender phoretic theory (SPT) is not only fully three-dimensional, but also algebraically accurate to first order in the filament slenderness. An interesting outcome of this analysis is that only centreline curvature, and not torsion, can have this leading-order effect on the dynamics.

We will focus herein on the derivation of this theory, its validation and the resultant analytical insights that arise, rather than the potential computational gains of our theory. The paper is organised as follows. In § 2, we present the slender phoretic theory to obtain the surface distribution of chemical for a slender filament of arbitrary 3-D centreline and surface chemical properties. This theory is then coupled to the recent slender body theory of Koens & Lauga (2018) to obtain the filament's swimming velocity. Section 3 outlines the numerical solution of the resulting integral equation. In § 4, we validate our leading-order concentration field against analytical results for straight prolate spheroids, and in § 5 we validate the first-order concentration calculation for curved planar filaments. In § 6, we examine further the change in the dynamics from excluding azimuthal slip flows to curved planar filaments. Section 7 demonstrates the 3-D capability of the theory with the simple test case of an autophoretic helix, while § 8 concludes with a discussion.

2. Slender phoretic theory

2.1. *Autophoretic propulsion*

A phoretic swimmer achieves propulsion by catalysing a chemical reaction in the surrounding solute fuel, denoted by its 'activity' $\mathcal{A}(\boldsymbol{x})$, for $\boldsymbol{x}$ a point on the swimmer surface. The activity represents concentration flux and may vary across the swimmer, with $\mathcal{A} > 0$, $\mathcal{A} < 0$ corresponding to release and or consumption of solute respectively. Local concentration gradients arise from spatial variation in the activity and confinement effects. These gradients result in local pressure imbalances in a thin boundary layer at the swimmer surface, driving a surface slip flow (Anderson 1989; Michelin & Lauga 2014). This slip flow is locally proportional to the concentration gradient, with the swimmer's 'mobility' $\mathcal{M}(\boldsymbol{x})$ as the (spatially varying) constant of proportionality. The mobility may be positive or negative, depending on whether the slip flow moves up or down the concentration gradient.

We consider neutral solute self-diffusiophoresis, where electrokinetic effects are absent (Brown & Poon 2014; Ebbens *et al.* 2014), and work in the limit of zero Péclet number (Golestanian, Liverpool & Ajdari 2007) where diffusion dominates and advection of the solute due to flow can be neglected. This limit is appropriate provided that the particle is smaller than $r_c = D/U$, for D solute diffusivity and U the typical phoretic velocity (Michelin & Lauga 2014). For platinum-coated Janus particles in hydrogen peroxide solution, this critical radius corresponds to $r_c \approx 10$–$100 \ \mu m$ (Howse *et al.* 2007). For a detailed discussion of propulsion at finite Péclet number, see Michelin & Lauga (2014).

At zero Péclet number, the solute dynamics decouples from the flow dynamics at any instant, so that the concentration field $c(\boldsymbol{x}, t)$ is found by solving Laplace's equation

$$D\nabla^2 c = 0, \tag{2.1}$$

in the region outside the swimmer, with surface S, subject to the boundary condition

$$-D\boldsymbol{n}_f \boldsymbol{\cdot} \nabla c|_S = \mathcal{A}(\boldsymbol{x})|_S, \tag{2.2}$$

with $\boldsymbol{n}_f$ the outward normal to the swimmer's surface, pointing into the fluid, and D the solute diffusivity. The solution of the diffusion problem is then used to calculate the surface slip velocity,

$$\boldsymbol{v}_{slip}|_S = \mathcal{M}(\boldsymbol{x})(\boldsymbol{1} - \boldsymbol{n}_f \boldsymbol{n}_f) \boldsymbol{\cdot} \nabla c, \tag{2.3}$$

Problem set-up

$$-D\boldsymbol{n}_f \cdot \nabla c|_S = \mathcal{A}(\boldsymbol{x})|_S \;\rightarrow\; D\nabla^2 c = 0 \;\rightarrow\; \boldsymbol{v}_{slip} = \mathcal{M}(\boldsymbol{x})(1 - \boldsymbol{n}_f \boldsymbol{n}_f) \cdot \nabla c \;\rightarrow\; \begin{array}{l} \mu \nabla^2 u = \nabla p \\ \nabla \cdot \boldsymbol{u} = 0 \end{array}$$

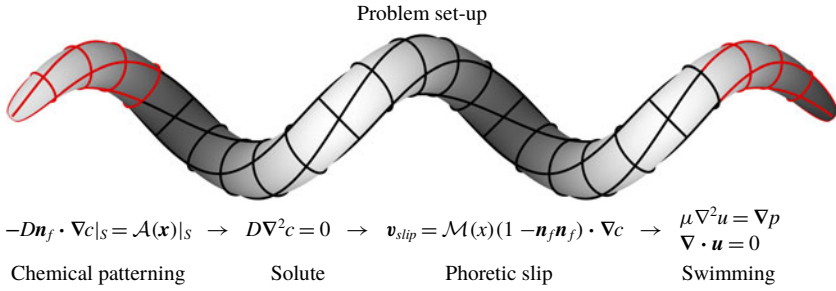Chemical patterning   Solute   Phoretic slip   Swimming

FIGURE 1. A schematic of a slender phoretic filament in three dimensions, in the shape of a helix. Surface lines are used to emphasise curvature and torsion. Laplace's equation is solved in the bulk, with flux boundary condition on the surface of the filament S determined by its activity $\mathcal{A}(\boldsymbol{x})|_S$. In later examples, we consider axisymmetric activity in the form of catalytic end caps (demarcated here by the red) with an inert midpiece, so that $\mathcal{A}(s) = -1$, $|s| > s_c$, $\mathcal{A}(s) = 0$ otherwise.

which gives the body-frame boundary conditions for solving the Stokes flow problem

$$\mu \nabla^2 \boldsymbol{u} - \nabla p = \boldsymbol{0}, \quad \nabla \cdot \boldsymbol{u} = 0. \tag{2.4}$$

This slip flow will in general propel the swimmer with translational velocity $\boldsymbol{U}_{sw}$, and angular velocity $\boldsymbol{\Omega}_{sw}$, which are found by enforcing the constraints that no net force or torque acts on the swimmer.

Thus, given an activity and mobility, the task of this paper is to find a convenient slender body approximation for the concentration field, and slip flow that results from its surface gradient. This flow will drive the kinematics of the filament, which will change depending on its centreline shape. The set-up of the problem and governing equations are shown in figure 1.

2.2. *Filament geometry*

We begin by describing the filament geometry, following the approach of Koens & Lauga (2018). The filament centreline $\boldsymbol{r}(s)$ is parametrised by its arclength $s \in [-l, l]$, where $2l$ is the total contour length. The centreline tangent $\hat{\boldsymbol{t}}(s)$, normal $\hat{\boldsymbol{n}}(s)$, and binormal $\hat{\boldsymbol{b}}(s)$ satisfy the Serret–Frenet equations,

$$\frac{\partial \hat{\boldsymbol{t}}}{\partial s} = \kappa \hat{\boldsymbol{n}}, \quad \frac{\partial \hat{\boldsymbol{n}}}{\partial s} = -\kappa \hat{\boldsymbol{t}} + \tau \hat{\boldsymbol{b}}, \quad \frac{\partial \hat{\boldsymbol{b}}}{\partial s} = -\tau \hat{\boldsymbol{n}}, \tag{2.5a-c}$$

where $\kappa(s)$ and $\tau(s)$ are the curvature and torsion of the filament centreline, respectively.

2.2.1. *Parametrising the surface*

The filament cross-sectional radius, which may vary along the filament, takes the value $r_f \rho(s)$ at s, where r_f is the maximal radius and $\rho(s) \in [0, 1]$. The surface of the filament is then parametrised by s, $r_f \rho(s)$, and the azimuthal angle of the cross-section, $\theta \in [-\pi, \pi]$, by

$$\boldsymbol{S}(s, \theta) = \boldsymbol{r}(s) + r_f \rho(s)\hat{\boldsymbol{e}}_\rho(s, \theta). \tag{2.6}$$

The local radial unit vector perpendicular to the centreline tangent, $\hat{\boldsymbol{e}}_\rho(s, \theta)$, is given by

$$\hat{\boldsymbol{e}}_\rho(s, \theta) = \cos \theta_m(s, \theta)\hat{\boldsymbol{n}}(s) + \sin \theta_m(s, \theta)\hat{\boldsymbol{b}}(s), \tag{2.7}$$

where $\theta_m(s, \theta) = \theta - \theta_i(s)$, with $\theta_i(s)$, accounting for the torsion of the curve, chosen to satisfy

$$\frac{\partial \theta_i}{\partial s} = \tau(s), \tag{2.8}$$

as in Koens & Lauga (2018). With this choice, the derivative of $\hat{\boldsymbol{e}}_\rho$ with respect to s simplifies to

$$\frac{\partial \hat{\boldsymbol{e}}_\rho}{\partial s} = -\kappa(s) \cos \theta_m(s, \theta)\hat{\boldsymbol{t}}(s). \tag{2.9}$$

2.2.2. *Surface elements*

To obtain the surface element, used later in our integrals, we calculate the derivatives

$$\frac{\partial \boldsymbol{S}}{\partial s} = \hat{\boldsymbol{t}}(s)[1 - r_f \rho(s)\kappa(s) \cos \theta_m(s, \theta)]$$
$$+ r_f \frac{\mathrm{d}\rho(s)}{\mathrm{d}s}[\cos \theta_m(s, \theta)\hat{\boldsymbol{n}}(s) + \sin \theta_m(s, \theta)\hat{\boldsymbol{b}}(s)], \tag{2.10a}$$

$$\frac{\partial \boldsymbol{S}}{\partial \theta} = r_f \rho(s)[-\sin \theta_m(s, \theta)\hat{\boldsymbol{n}}(s) + \cos \theta_m(s, \theta)\hat{\boldsymbol{b}}(s)], \tag{2.10b}$$

which gives the surface element as

$$\frac{\partial \boldsymbol{S}}{\partial s} \times \frac{\partial \boldsymbol{S}}{\partial \theta} = r_f \rho(s) \left(r_f \frac{\mathrm{d}\rho(s)}{\mathrm{d}s}\hat{\boldsymbol{t}}(s) - [1 - r_f \rho(s)\kappa(s) \cos \theta_m(s, \theta)]\hat{\boldsymbol{e}}_\rho(s, \theta) \right), \tag{2.11}$$

with magnitude

$$\left| \frac{\partial \boldsymbol{S}}{\partial s} \times \frac{\partial \boldsymbol{S}}{\partial \theta} \right| = r_f \rho(s) \sqrt{\left[r_f \frac{\mathrm{d}\rho(s)}{\mathrm{d}s} \right]^2 + [1 - r_f \rho(s)\kappa(s) \cos \theta_m(s, \theta)]^2}. \tag{2.12}$$

2.3. *Boundary integral equation for the diffusion equation*

We begin with the well-known Green's function for Laplace's equation in an unconfined, three-dimensional region,

$$\mathcal{G}(\boldsymbol{x}, \tilde{\boldsymbol{x}}) = \frac{1}{4\pi|\boldsymbol{x} - \tilde{\boldsymbol{x}}|}, \tag{2.13}$$

which solves Laplace's equation, forced by a point sink at $\tilde{\boldsymbol{x}}$,

$$\nabla^2 \mathcal{G}(\boldsymbol{x}, \tilde{\boldsymbol{x}}) = -\delta(\boldsymbol{x} - \tilde{\boldsymbol{x}}). \tag{2.14}$$

Since in our unbounded domain we have translational invariance, we use the notation $\mathcal{G}(\boldsymbol{x}, \tilde{\boldsymbol{x}}) = \mathcal{G}(\boldsymbol{x} - \tilde{\boldsymbol{x}}) = 1/4\pi|\boldsymbol{R}|$, where $\boldsymbol{R} = \boldsymbol{x} - \tilde{\boldsymbol{x}}$.

Using Green's second identity for the functions $c(\tilde{\boldsymbol{x}})$ and $\mathcal{G}(\tilde{\boldsymbol{x}} - \boldsymbol{x})$, in the body of the fluid outside the filament V, bounded by filament surface S, with normal $\boldsymbol{n}_f$ pointing out of the filament, and the notation $\partial/\partial n_f = \boldsymbol{n}_f \cdot \nabla_{\tilde{\boldsymbol{x}}}$, we have

$$\int_V (c(\tilde{\boldsymbol{x}})\nabla_{\tilde{\boldsymbol{x}}}^2 \mathcal{G}(\tilde{\boldsymbol{x}} - \boldsymbol{x}) - \mathcal{G}(\tilde{\boldsymbol{x}} - \boldsymbol{x})\nabla_{\tilde{\boldsymbol{x}}}^2 c(\tilde{\boldsymbol{x}})) \, \mathrm{d}V(\tilde{\boldsymbol{x}})$$
$$= -\int_S \left(c(\tilde{\boldsymbol{x}})\boldsymbol{n}_f \cdot \frac{\partial \mathcal{G}(\tilde{\boldsymbol{x}} - \boldsymbol{x})}{\partial \tilde{\boldsymbol{x}}} - \mathcal{G}(\tilde{\boldsymbol{x}} - \boldsymbol{x})\boldsymbol{n}_f \cdot \frac{\partial c(\tilde{\boldsymbol{x}})}{\partial \tilde{\boldsymbol{x}}} \right) \mathrm{d}S(\tilde{\boldsymbol{x}}), \tag{2.15}$$

which simplifies to the classic boundary integral formulation

$$\lambda c(\boldsymbol{x}) = \frac{1}{4\pi} \int_S \left[\frac{c(\tilde{\boldsymbol{x}})\boldsymbol{n}_f \cdot (\boldsymbol{x} - \tilde{\boldsymbol{x}})}{|\boldsymbol{x} - \tilde{\boldsymbol{x}}|^3} + \frac{\mathcal{A}(\tilde{\boldsymbol{x}})}{D|\boldsymbol{x} - \tilde{\boldsymbol{x}}|} \right] \mathrm{d}S(\tilde{\boldsymbol{x}}), \tag{2.16}$$

where $\lambda = 1/2$ for $\boldsymbol{x} \in S$, $\lambda = 1$ for $\boldsymbol{x} \in V$, and $\lambda = 0$ for $\boldsymbol{x} \notin V$ (Pozrikidis 1992).

We now substitute the filament geometry into (2.16). For $\boldsymbol{x} = \boldsymbol{S}(s, \theta)$ and $\tilde{\boldsymbol{x}} = \boldsymbol{S}(\tilde{s}, \tilde{\theta})$ points on the filament surface, we set $\lambda = 1/2$, and using the notation,

$$\boldsymbol{R} \equiv \boldsymbol{S}(s, \theta) - \boldsymbol{S}(\tilde{s}, \tilde{\theta}) = \boldsymbol{R}_0(s, \tilde{s}) + r_f[\rho(s)\hat{\boldsymbol{e}}_\rho(s, \theta) - \rho(\tilde{s})\hat{\boldsymbol{e}}_\rho(\tilde{s}, \tilde{\theta})], \tag{2.17}$$

with $\boldsymbol{R}_0 \equiv \boldsymbol{r}(s) - \boldsymbol{r}(\tilde{s})$, and $\boldsymbol{n}_f \, \mathrm{d}S_{\tilde{\boldsymbol{x}}} = -(\partial \boldsymbol{S}/\partial \tilde{s}) \times (\partial \boldsymbol{S}/\partial \tilde{\theta}) \, \mathrm{d}\tilde{\theta} \, \mathrm{d}\tilde{s}$ (where the sign is due to definition of $\boldsymbol{n}_f$ pointing out of the filament), we can write (2.16) as

$$2\pi c(s, \theta) = \int_{-l}^{l} \int_{-\pi}^{\pi} \left[\frac{\mathcal{A}(\tilde{s}, \tilde{\theta})}{D|\boldsymbol{R}|} \left| \frac{\partial \boldsymbol{S}}{\partial \tilde{s}} \times \frac{\partial \boldsymbol{S}}{\partial \tilde{\theta}} \right| - \frac{c(\tilde{s}, \tilde{\theta})\boldsymbol{R}}{|\boldsymbol{R}|^3} \cdot \left(\frac{\partial \boldsymbol{S}}{\partial \tilde{s}} \times \frac{\partial \boldsymbol{S}}{\partial \tilde{\theta}} \right) \right] \mathrm{d}\tilde{\theta} \, \mathrm{d}\tilde{s}, \tag{2.18}$$

with the surface element and its magnitude given by (2.11) and (2.12) respectively.

While the boundary integral (2.18) now includes the filament geometry, it does not yet use the approximation that the filament is slender. This approximation will allow us, after performing matched asymptotics (details in the appendices), to write the double integral equation (2.18) into a single integral formula for evaluating the concentration on the filament surface.

We non-dimensionalise lengths by r_f, activity by a typical activity $[\mathcal{A}]$ and concentration by a typical concentration $[c]$ taken as $[c] \equiv [\mathcal{A}]r_f/D$. The last choice comes from considering the boundary condition $-D\boldsymbol{n}_f \cdot \nabla c|_S = \mathcal{A}|_S$, and noting that, since $\boldsymbol{n}_f$ is mostly aligned with $\hat{\boldsymbol{e}}_\rho$, $\boldsymbol{n}_f \cdot \nabla c$ scales as $[c]/r_f$. For a typical mobility scale $[\mathcal{M}]$, using that $[c] \sim [\mathcal{A}]r_f/D$, and scaling $\boldsymbol{v}_{slip} \sim [\mathcal{M}][\mathcal{A}]r_f/(Dl)$, (i.e. $[\partial c/\partial s] \sim [c]/l$). All quantities are henceforth non-dimensional, unless otherwise stated.

2.4. *Azimuthal versus longitudinal slip flows in the slender limit*

Before deriving the slender body approximation of (2.18), we sketch out the relevant terms in the theory, and the assumptions we will make. Defining $\epsilon = r_f/l$, the slenderness parameter, we are interested in the leading-order swimming velocity, which is determined by the leading-order slip velocity.

For the majority of the filament, this slip velocity is equal to $\mathcal{M}\partial c/\partial s$ longitudinally, and $\mathcal{M}(\epsilon\rho)^{-1}\partial c/\partial\theta$ azimuthally. For non-axisymmetric chemical patterning $\mathcal{A}(s, \theta)$, we might expect variations of $c(s, \theta)$ in s and θ to be of the same order, so that azimuthal slip flows will be $O(\epsilon^{-1})$ and dominate the dynamics.

For axisymmetric chemical patterning $\mathcal{A}(s)$, a straight rod will have no azimuthal concentration variation, by symmetry. However, a curved rod will have small azimuthal variations in concentration arising from geometric confinement. We will show that these variations are in general $O(\epsilon)$, and as a consequence contribute to the slip flow at the same order as $\partial c/\partial s$. As such, a consistent leading-order SPT expansion of the velocity requires $O(\epsilon)$ expansion of the concentration field, in contrast to other slender body theories (Johnson 1979; Götz 2000; Yariv 2008; Schnitzer & Yariv 2015; Ibrahim *et al.* 2017; Koens & Lauga 2018; Yariv 2019).

For the derivation of the following theory, we will assume that the activity $\mathcal{A}(s, \theta)$ and curvature $\kappa(s)$ of the filament are slowly varying with s. We will also assume that either the filament as prolate spheroidal cross-section $\rho(s) = \sqrt{(1 - s^2)}$, or the activity

is zero near the filament ends. From a practical calculation standpoint, our validation against boundary element simulation will demonstrate that these assumptions can often be relaxed. Finally, to allow a convenient decomposition of the azimuthal slip velocity into modes, for simple use in the slender body theory of Koens & Lauga (2018), we will also assume axisymmetric mobility $\mathcal{M}(s)$, though this assumption does not come into the derivation of the slender phoretic theory itself.

2.5. *Asymptotic expansion of the boundary integral kernels*

The surface element from (2.11), now in its non-dimensionalised form,

$$\frac{\partial \boldsymbol{S}}{\partial \tilde{s}} \times \frac{\partial \boldsymbol{S}}{\partial \tilde{\theta}} = \epsilon \rho \left(-\hat{\boldsymbol{e}}_\rho(\tilde{s}, \tilde{\theta}) + \epsilon \left[\frac{\mathrm{d}\rho(\tilde{s})}{\mathrm{d}\tilde{s}} \hat{\boldsymbol{t}}(\tilde{s}) + \rho(\tilde{s})\kappa(\tilde{s}) \cos\theta_m(\tilde{s}, \tilde{\theta}) \hat{\boldsymbol{e}}_\rho(\tilde{s}, \tilde{\theta}) \right] \right), \quad (2.19)$$

has magnitude

$$\left| \frac{\partial \boldsymbol{S}}{\partial \tilde{s}} \times \frac{\partial \boldsymbol{S}}{\partial \tilde{\theta}} \right| = \epsilon \rho(\tilde{s}) \sqrt{\epsilon^2 \left(\frac{\mathrm{d}\rho(\tilde{s})}{\mathrm{d}\tilde{s}} \right)^2 + [1 - \epsilon \rho(\tilde{s})\kappa(\tilde{s}) \cos\theta_m(\tilde{s}, \tilde{\theta})]^2}$$

$$= \epsilon \rho(\tilde{s})[1 - \epsilon \rho(\tilde{s})\kappa(\tilde{s}) \cos\theta_m(\tilde{s}, \tilde{\theta}) + O(\epsilon^2)]. \quad (2.20)$$

The non-dimensionalised version of the boundary integral expression of (2.18) is

$$2\pi c(s, \theta) = \int_{-1}^{1} \int_{-\pi}^{\pi} [K_1(s, \theta, \tilde{s}, \tilde{\theta}) + K_2(s, \theta, \tilde{s}, \tilde{\theta})] \, \mathrm{d}\tilde{\theta} \, \mathrm{d}\tilde{s}, \quad (2.21)$$

with the two kernels $K_1(s, \tilde{s}, \theta, \tilde{\theta})$, $K_2(s, \tilde{s}, \theta, \tilde{\theta})$ defined as

$$K_1 = \frac{\rho(\tilde{s})\mathcal{A}(\tilde{s}, \tilde{\theta})}{|\boldsymbol{R}|} \quad [1 - \epsilon \rho(\tilde{s})\kappa(\tilde{s}) \cos\theta_m(\tilde{s}, \tilde{\theta}) + O(\epsilon^2)], \quad (2.22a)$$

$$K_2 = \epsilon \frac{\rho(\tilde{s})c(\tilde{s}, \tilde{\theta})}{|\boldsymbol{R}|^3} \boldsymbol{R} \cdot \left(\hat{\boldsymbol{e}}_\rho(\tilde{s}, \tilde{\theta}) - \epsilon \left[\frac{\mathrm{d}\rho(\tilde{s})}{\mathrm{d}\tilde{s}} \hat{\boldsymbol{t}}(\tilde{s}) + \rho(\tilde{s})\kappa(\tilde{s}) \cos\theta_m(\tilde{s}, \tilde{\theta}) \hat{\boldsymbol{e}}_\rho(\tilde{s}, \tilde{\theta}) \right] \right). \quad (2.22b)$$

In the slender limit where ϵ is small, for each evaluation parameter s two regions of the integration variable $\tilde{s}$ arise, according to how $\tilde{s} - s$ compares to ϵ. In the outer region, $\tilde{s} - s = O(1)$, the integration variable is far away from the evaluation arclength parameter. In the inner region, $\tilde{s} - s = O(\epsilon)$, the integration variable is within ϵ arclength distance from the evaluation arclength. We proceed with a matched-asymptotic expansion of the integral kernels prior to their integration.

2.5.1. *Outer region*

In the outer region, $s - \tilde{s} = O(1)$, hence $\boldsymbol{R}_0(s, \tilde{s}) = O(1)$, so we can approximate $\boldsymbol{R} \approx \boldsymbol{R}_0$. To first order,

$$\boldsymbol{R} = \boldsymbol{R}_0(s, \tilde{s}) + \epsilon \mathcal{D}_{(\tilde{s}, \tilde{\theta})}^{(s, \theta)}, \quad (2.23)$$

where

$$\mathcal{D}_{(\tilde{s}, \tilde{\theta})}^{(s, \theta)} \equiv \rho(s)\hat{\boldsymbol{e}}_\rho(s, \theta) - \rho(\tilde{s})\hat{\boldsymbol{e}}_\rho(\tilde{s}, \tilde{\theta}). \quad (2.24)$$

Expanding and collecting the orders of ϵ (see § A.1 for details), gives the outer expansions $K_1^{(o)}$, $K_2^{(o)}$ of the kernels K_1, K_2, defined in (2.22a)–(2.22b), as

$$K_1^{(o)} = \frac{\rho(\tilde{s})\mathcal{A}(\tilde{s}, \tilde{\theta})}{|\boldsymbol{R}_0(s, \tilde{s})|} \left(1 - \epsilon \left[\rho(\tilde{s})\kappa(\tilde{s}) \cos\theta_m(\tilde{s}, \tilde{\theta}) + \frac{\boldsymbol{R}_0}{|\boldsymbol{R}_0|^2} \cdot \mathcal{D}_{(\tilde{s}, \tilde{\theta})}^{(s, \theta)} \right] + O(\epsilon^2) \right), \quad (2.25)$$

$$K_2^{(o)} = \epsilon \frac{\rho(\tilde{s})c(\tilde{s}, \tilde{\theta})}{|\boldsymbol{R}_0|^3} \left(\boldsymbol{R}_0 \cdot \hat{\boldsymbol{e}}_\rho(\tilde{s}, \tilde{\theta}) + \epsilon(\boldsymbol{\mathcal{D}}_{(\tilde{s}, \tilde{\theta})}^{(s,\theta)}) \cdot \hat{\boldsymbol{e}}_\rho(\tilde{s}, \tilde{\theta}) \right.$$

$$- \epsilon \boldsymbol{R}_0 \cdot \left[\frac{\mathrm{d}\rho(\tilde{s})}{\mathrm{d}\tilde{s}} \hat{\boldsymbol{t}}(\tilde{s}) + \rho(\tilde{s})\kappa(\tilde{s}) \cos \theta_m(\tilde{s}, \tilde{\theta}) \hat{\boldsymbol{e}}_\rho(\tilde{s}, \tilde{\theta}) \right]$$

$$\left. - \epsilon(\boldsymbol{R}_0 \cdot \hat{\boldsymbol{e}}_\rho(\tilde{s}, \tilde{\theta})) \frac{3\boldsymbol{R}_0 \cdot \boldsymbol{\mathcal{D}}_{(\tilde{s}, \tilde{\theta})}^{(s,\theta)}}{|\boldsymbol{R}_0|^2} + O(\epsilon^2) \right). \tag{2.26}$$

2.5.2. *Inner region*

In the inner region, $s - \tilde{s} = O(\epsilon)$, and we let $\tilde{s} = s + \epsilon \chi$, where χ is $O(1)$. The expansion and calculation, which we will now summarise, are given in detail in § A.2. Taylor expanding functions of $\tilde{s}$ around s (for example, $\rho(\tilde{s}) = \rho(s) + \epsilon \chi \, \mathrm{d}\rho(s)/\mathrm{d}s + O(\epsilon^2)$) gives the inner approximation for (2.17) as

$$\boldsymbol{R} = \epsilon[\hat{\boldsymbol{R}}_{(i)}^{(1)} + \epsilon \hat{\boldsymbol{R}}_{(i)}^{(2)}] + O(\epsilon^3), \tag{2.27}$$

where

$$\hat{\boldsymbol{R}}_{(i)}^{(1)} = -\chi \hat{\boldsymbol{t}}(s) + \rho(s)[\hat{\boldsymbol{e}}_\rho(s, \theta) - \hat{\boldsymbol{e}}_\rho(s, \tilde{\theta})], \tag{2.28a}$$

$$\hat{\boldsymbol{R}}_{(i)}^{(2)} = -\left[\frac{1}{2} \chi^2 \kappa \hat{\boldsymbol{n}}(s) + \chi \frac{\mathrm{d}\rho(s)}{\mathrm{d}s} \hat{\boldsymbol{e}}_\rho(s, \tilde{\theta}) - \chi \rho(s)\kappa(s) \cos \theta_m(s, \tilde{\theta}) \hat{\boldsymbol{t}}(s) \right], \tag{2.28b}$$

$$|\hat{\boldsymbol{R}}_{(i)}^{(1)} + \epsilon \hat{\boldsymbol{R}}_{(i)}^{(2)}| = |\hat{\boldsymbol{R}}_{(i)}^{(1)}|[1 + \epsilon \hat{\boldsymbol{R}}_{(i)}^{(1)} \cdot \hat{\boldsymbol{R}}_{(i)}^{(2)}/|\hat{\boldsymbol{R}}_{(i)}^{(1)}|^2 + O(\epsilon^2)]. \tag{2.28c}$$

Noting that

$$|\hat{\boldsymbol{R}}_{(i)}^{(1)}| = \sqrt{\chi^2 + \gamma^2}, \tag{2.29}$$

with

$$\gamma^2 = 2\rho^2(s)[1 - \cos(\theta - \tilde{\theta})], \tag{2.30}$$

the expansion of $1/|\boldsymbol{R}|$ will give rise to a factor $1/\sqrt{\chi^2 + \gamma^2}$. As a result, powers of $1/\sqrt{\chi^2 + \gamma^2}$ with different exponents appear in different terms of the expression of $K_1^{(i)}$, $K_2^{(i)}$, given in § A.2.2.

Performing the integration in $\tilde{s}$, we treat the integrals of the form $I_j^i = \int_{-1}^{1} (\chi^i/\epsilon \sqrt{\chi^2 + \gamma^2}^j) \, \mathrm{d}\tilde{s}$, where i, j positive constants, as in Koens & Lauga (2018), see § A.2.3. Some of these integrals give rise to logarithmic terms, and we arrive at

$$\int_{-1}^{1} K_1^{(i)} \, \mathrm{d}\tilde{s} = \rho(s)\mathcal{A}(s, \tilde{\theta}) \log \left(\frac{2(1 - s^2)}{\epsilon^2 \rho^2(s)[1 - \cos(\theta - \tilde{\theta})]} \right) - 2s\partial_s[\rho(s)\mathcal{A}(s, \tilde{\theta})]$$

$$+ \epsilon \left\{ -\mathcal{A}(s, \tilde{\theta})\rho^2(s)\kappa(s) \cos \theta_m(s, \tilde{\theta}) \log \left(\frac{2(1 - s^2)}{\epsilon^2 \rho^2(s)[1 - \cos(\theta - \tilde{\theta})]} \right) \right.$$

$$+ \rho^2(s)\mathcal{A}(s, \tilde{\theta}) \frac{1}{2}\kappa(s)[\cos \theta_m(s, \tilde{\theta}) + \cos \theta_m(s, \theta)]$$

$$\times \left[\log \left(\frac{2(1 - s^2)}{\epsilon^2 \rho^2(s)[1 - \cos(\theta - \tilde{\theta})]} \right) - 2 \right] \right\}$$

$$+ \frac{2s\epsilon^2}{s^2 - 1} \rho^2(s)\mathcal{A}(s, \tilde{\theta}) \frac{\mathrm{d}\rho(s)}{\mathrm{d}s}[\cos(\theta - \tilde{\theta}) - 1] + O(\epsilon^2), \tag{2.31}$$

$$\int_{-1}^{1} K_2{}^{(i)} \, d\tilde{s} = -c(s, \tilde{\theta})$$

$$+ \frac{1}{2}\epsilon c(s, \tilde{\theta}) \left[\log \left(\frac{2(1 - s^2)}{\epsilon^2 \rho^2(s)[1 - \cos(\theta - \tilde{\theta})]} \right) \right] \kappa(s)\rho(s) \cos \theta_m(s, \tilde{\theta})$$

$$- \epsilon c(s, \tilde{\theta}) \frac{1}{2} \rho(s)\kappa(s)[\cos \theta_m(s, \tilde{\theta}) + \cos \theta_m(s, \theta)]$$

$$+ \frac{2s\epsilon^2}{s^2 - 1} \rho(s)[\cos(\theta - \tilde{\theta}) - 1]\partial_s[\rho(s)c(s, \tilde{\theta})] + O(\epsilon^2 c). \tag{2.32}$$

While terms incorporating the fraction $2\epsilon^2(s\rho^2(s)/(s^2 - 1))(d\rho(s)/ds)$ are $O(\epsilon^2)$, we have written them explicitly above as they generally diverge as $s \to \pm 1$, and can thus become leading order in a very small region ϵ^2 from the ends. This divergence can be circumvented by assuming a prolate spheroidal shape filament $\rho(s) \sim \sqrt{1 - s^2}$, or ensuring the activity $\mathcal{A}$ decays to zero at either end. For a more detailed scaling argument, see appendix C.

2.5.3. *Matching: common part*

We follow the van Dyke matching method, and use $\epsilon \chi = \tilde{s} - s$ expanding the inner region in terms of the outer region variable $\tilde{s}$, and the outer region in terms of the inner variable χ, and finding the common part, expected to be the same, by expanding in ϵ. We use the superscripts $(i) \in (o)$ for the expansion of the inner region kernel in terms of the outer variable, and $(o) \in (i)$ for the expansion of the outer region kernel in terms of the inner variable.

In order to obtain $K_1{}^{(o)\in(i)}$ and $K_2{}^{(o)\in(i)}$, we substitute $\tilde{s} = s + \epsilon \chi$ in the expressions for $K_1{}^{(o)}$ and $K_2{}^{(o)}$ and expand. The resulting expressions for $K_1{}^{(o)\in(i)}$ and $K_2{}^{(o)\in(i)}$ are given in § A.3 (we note that these are the same as for $K_1{}^{(i)\in(o)}$, $K_2{}^{(i)\in(o)}$, as expected). Following integration,

$$\int_{-1}^{1} \int_{-\pi}^{\pi} K_1{}^{(o)\in(i)} \, d\tilde{s} \, d\tilde{\theta} = \int_{-1}^{1} \frac{\rho(s)}{|\tilde{s} - s|} \int_{-\pi}^{\pi} \mathcal{A}(s, \tilde{\theta}) \, d\tilde{\theta} \, d\tilde{s} - 2s\partial_s \int_{-\pi}^{\pi} [\rho(s)\mathcal{A}(s, \tilde{\theta})] \, d\tilde{\theta}$$

$$- \frac{1}{2}\epsilon \rho^2(s)\kappa(s) \int_{-1}^{1} \frac{1}{|\tilde{s} - s|} \int_{-\pi}^{\pi} \mathcal{A}(s, \tilde{\theta})$$

$$\times [\cos \theta_m(s, \tilde{\theta}) - \cos \theta_m(s, \theta)] \, d\tilde{\theta} \, d\tilde{s} + O(\epsilon^2), \tag{2.33}$$

$$\int_{-1}^{1} \int_{-\pi}^{\pi} K_2{}^{(o)\in(i)} \, d\tilde{s} \, d\tilde{\theta} = O(\epsilon^2). \tag{2.34}$$

2.5.4. *Composite solution*

The boundary integral (2.18) is approximated by adding the outer and inner expansions and subtracting from each the common part,

$$2\pi c(s, \theta) \approx \int_{-1}^{1} \int_{-\pi}^{\pi} (K_1{}^{(o)} + K_1{}^{(i)} - K_1{}^{(i)\in(o)} + K_2{}^{(o)} + K_2{}^{(i)} - K_2{}^{(i)\in(o)}) \, d\tilde{\theta} \, d\tilde{s}. \tag{2.35}$$

The full expansion for the concentration field is given in § B.1. We now use the notation $c^{(0)}$ and $c^{(1)}$ for the leading- and first-order algebraic corrections of c,

$$c = c^{(0)} + \epsilon c^{(1)} + O(\epsilon^2), \tag{2.36}$$

and consider each in turn. The leading order includes all terms of $O(1)$ and $O(\log \epsilon)$. The correction to the leading order, $\epsilon c^{(1)}$, vanishes as $\epsilon \to 0$, and includes both $O(\epsilon)$ and $O(\epsilon \log \epsilon)$. The details of simplifications are given in §§ B.2 and B.3. We now present the resulting expressions.

2.6. *Leading-order concentration field*

Writing $\langle f(s) \rangle \equiv \int_{-\pi}^{\pi} f(s, \tilde{\theta}) \, d\tilde{\theta}$, the leading-order expression for the concentration field (originating from (B 2) in § B.2) is given by

$$2\pi c^{(0)}(s, \theta) + \langle c^{(0)}(s) \rangle = + \int_{-1}^{1} \left[\frac{\rho(\tilde{s})\langle \mathcal{A}(\tilde{s}) \rangle}{|\boldsymbol{R}_0(s, \tilde{s})|} - \frac{\rho(s)\langle \mathcal{A}(s) \rangle}{|\tilde{s} - s|} \right] d\tilde{s}$$
$$+ \rho(s)\langle \mathcal{A}(s) \rangle \log \left(\frac{2(1 - s^2)}{\epsilon^2 \rho^2(s)} \right)$$
$$- \rho(s) \int_{-\pi}^{\pi} \mathcal{A}(s, \tilde{\theta}) \log[1 - \cos(\theta - \tilde{\theta})] \, d\tilde{\theta}. \qquad (2.37)$$

Integrating this again over θ allows us to evaluate $\langle c^{(0)}(s) \rangle$ and then subtract it from (2.37), the details of which are given in § B.2. We thus arrive at the leading-order slender boundary integral equation

$$4\pi c^{(0)}(s, \theta) = \int_{-1}^{1} \left[\frac{\rho(\tilde{s})\langle \mathcal{A}(\tilde{s}) \rangle}{|\boldsymbol{R}_0(s, \tilde{s})|} - \frac{\rho(s)\langle \mathcal{A}(s) \rangle}{|\tilde{s} - s|} \right] d\tilde{s} + \rho(s)\langle \mathcal{A}(s) \rangle \log \left(\frac{(1 - s^2)}{\epsilon^2 \rho^2(s)} \right)$$
$$- 2\rho(s) \int_{-\pi}^{\pi} \mathcal{A}(s, \tilde{\theta}) \log[1 - \cos(\theta - \tilde{\theta})] \, d\tilde{\theta}. \qquad (2.38)$$

We thus see that for non-axisymmetric filaments, there is a leading-order contribution to the concentration that varies with θ. As such, we expect the slip velocity, and resulting dynamics, of such filaments, to be dominated by the final term in (2.38).

For filaments with axisymmetric activity, $\mathcal{A}(s, \theta) \equiv \mathcal{A}(s)$, and $\langle \mathcal{A}(s, \theta) \rangle = 2\pi \mathcal{A}(s)$, and using $\int_{-\pi}^{\pi} \log[1 - \cos(\theta - \tilde{\theta})] \, d\tilde{\theta} = -2\pi \log(2)$, we arrive at

$$2c^{(0)}(s, \theta) = + \int_{-1}^{1} \left[\frac{\rho(\tilde{s})\mathcal{A}(\tilde{s})}{|\boldsymbol{R}_0(s, \tilde{s})|} - \frac{\rho(s)\mathcal{A}(s)}{|\tilde{s} - s|} \right] d\tilde{s} + \rho(s)\mathcal{A}(s) \log \left(\frac{4(1 - s^2)}{\epsilon^2 \rho^2(s)} \right). \qquad (2.39)$$

The two terms inside the integrand of (2.39) both include non-local effects, while the logarithmic term, and the $\tilde{\theta}$ integral in the non-axisymmetric case (2.38), are local. Physically, equation (2.39) represents a line distribution of point sources located on the filament centreline, weighted by the filament activity and radius, with a local correction arising because we are evaluating the concentration on the filament.

Note that the terms of the integrand inside the square brackets both diverge when the integration variable $\tilde{s}$ passes through the evaluation arclength parameter s, however, the two singularities cancel each other, such that the integrand is regular. As explained in detail in Koens & Lauga (2018), the fraction inside the logarithmic term of (2.39) means that close to the endpoints, the cross-sectional radius $\rho(s)$ must decrease as $\sqrt{(1 - s^2)}$ (or less abruptly) for the logarithmic term not to diverge, i.e. the analysis is valid for prolate spheroidal ends.

2.7. *Next-order correction*

Equation (B 6) in § B.3 gives the full expression for $c^{(1)}(s, \theta)$ for a general activity $\mathcal{A}(s, \theta)$. Simplifying for the axisymmetric case $\mathcal{A}(s, \theta) \equiv \mathcal{A}(s)$, after some algebra (see § B.3) we finally arrive at

$$
2\pi c^{(1)}(s, \theta) + \langle c^{(1)}(s) \rangle = +\pi \rho^2(s) \kappa(s) \mathcal{A}(s) \cos \theta_m(s, \theta) \left[\log \left(\frac{4(1-s^2)}{\epsilon^2 \rho^2(s)} \right) - 3 \right]
$$
$$
- 2\pi \rho(s) \int_{-1}^{1} \rho(\tilde{s}) \mathcal{A}(\tilde{s}) \frac{\boldsymbol{R}_0}{|\boldsymbol{R}_0|^3} \, \mathrm{d}\tilde{s} \cdot \hat{\boldsymbol{e}}_\rho(s, \theta)
$$
$$
- \pi \rho^2(s) \kappa(s) \int_{-1}^{1} \frac{1}{|\tilde{s}-s|} \mathcal{A}(s) \cos \theta_m(s, \theta) \, \mathrm{d}\tilde{s}. \tag{2.40}
$$

Integrating over θ we see that $\langle c^{(1)}(s) \rangle = 0$, and the first-order correction to the slender boundary integral expression in the case of axisymmetric activity becomes

$$
2c^{(1)}(s, \theta) = \left[\log \left(\frac{4(1-s^2)}{\epsilon^2 \rho^2(s)} \right) - 3 \right] \rho^2(s) \kappa(s) \mathcal{A}(s) \cos[\theta - \theta_i(s)]
$$
$$
- \rho(s) \int_{-1}^{1} \left[\frac{2\rho(\tilde{s}) \mathcal{A}(\tilde{s}) \boldsymbol{R}_0 \cdot \hat{\boldsymbol{e}}_\rho(s, \theta)}{|\boldsymbol{R}_0|^3} + \frac{\rho(s) \kappa(s) \mathcal{A}(s) \cos[\theta - \theta_i(s)]}{|\tilde{s}-s|} \right] \mathrm{d}\tilde{s}. \tag{2.41}
$$

Importantly (though perhaps not obviously), the integral converges. This can be seen by substituting

$$
\boldsymbol{R}_0 = -(\tilde{s}-s) \left[\hat{\boldsymbol{t}}(s) + \tfrac{1}{2}(\tilde{s}-s)\kappa(s)\hat{\boldsymbol{n}}(s) + O((\tilde{s}-s)^2) \right], \tag{2.42}
$$

in the first fraction of the integrand, whereupon the leading-order term of the expansion of the first fraction of the integrand cancels the second term of the integrand, $\rho(s)\kappa(s)\mathcal{A}(s) \cos[\theta - \theta_i(s)]/|\tilde{s}-s|$, regularising the singularity. Physically, equation (2.41) represents a line distribution of source dipoles located on the filament centreline, weighted by the filament activity, radius and curvature, with a local correction.

Thus, for axisymmetric activity the full surface concentration is given (up to $O(\epsilon^2)$ corrections) by

$$
2c(s, \theta) = \int_{-1}^{1} \left[\frac{\rho(\tilde{s}) \mathcal{A}(\tilde{s})}{|\boldsymbol{R}_0(s, \tilde{s})|} - \frac{\rho(s) \mathcal{A}(s)}{|\tilde{s}-s|} \right] \mathrm{d}\tilde{s} + \rho(s) \mathcal{A}(s) \log \left(\frac{4(1-s^2)}{\epsilon^2 \rho^2(s)} \right)
$$
$$
+ \epsilon \left[\left[\log \left(\frac{4(1-s^2)}{\epsilon^2 \rho^2(s)} \right) - 3 \right] \rho^2(s) \kappa(s) \mathcal{A}(s) \cos[\theta - \theta_i(s)] \right.
$$
$$
\left. - \rho(s) \int_{-1}^{1} \left[\frac{2\rho(\tilde{s}) \mathcal{A}(\tilde{s}) \boldsymbol{R}_0 \cdot \hat{\boldsymbol{e}}_\rho(s, \theta)}{|\boldsymbol{R}_0|^3} + \frac{\rho(s) \kappa(s) \mathcal{A}(s) \cos[\theta - \theta_i(s)]}{|\tilde{s}-s|} \right] \mathrm{d}\tilde{s} \right]
$$
$$
+ O(\epsilon^2). \tag{2.43}
$$

In contrast to slender body equations for viscous flows, equation (2.43) is explicit; given the filament activity and geometry, one can directly calculate the concentration field by simply evaluating a line integral, rather than having to solve an integral

equation (cf. (2.22b), that has the concentration in the kernel K_2). Note further that, since we have non-dimensionalised with respect to the filament radius for asymptotic convenience, in order to make comparisons with existing results (non-dimensionalised with respect to the filament semiaxis), the entire solution must be premultiplied by ϵ.

We can now clearly see that there is azimuthal variation in the concentration field for curved axisymmetric filaments that is $O(\epsilon)$. As such, these azimuthal variations will in general have a leading-order effect on the filament swimming velocity. For a straight filament, all the $O(\epsilon)$ terms vanish in (2.43), which means that the leading-order expression for the concentration of a straight filament with axisymmetric activity is correct to $O(\epsilon^2)$.

This azimuthal dependence has a natural modal form in terms of $\sin[\theta - \theta_i(s)]$ and $\cos[\theta - \theta_i(s)]$, which will carry through as a modal expression for the phoretic slip velocity, and will naturally lead to a Fourier modes approach for the kinematics which we now describe.

2.8. *Slip velocity – azimuthal modes*

We now proceed to calculate the slip velocity for slender curved filaments with axisymmetric activity. In experimental systems, activity arises from deposition of catalyst at the surface, and so axisymmetric activity implies no azimuthal variation in surface chemistry. As such, we may also assume axisymmetric mobility $\mathcal{M}(s)$.

As in the above, the following analysis is not valid in a very small region $O(\epsilon^2)$ from the filament ends (typically 0.01 % of the total filament length for the examples we consider). The contribution to the dynamics from this region is discussed, and shown to be negligible, in appendix C. The leading-order slip velocity (2.3) for axisymmetric activity is given by

$$\boldsymbol{v}_{slip}(s, \theta) = \mathcal{M}(s) \left[\hat{\boldsymbol{t}}(s) \frac{\partial c^{(0)}}{\partial s} + \hat{\boldsymbol{e}}_\theta(s, \theta) \frac{1}{\rho(s)} \frac{\partial c^{(1)}}{\partial \theta} \right]. \tag{2.44}$$

Taking the θ-derivative of (2.43), we see that

$$\frac{2}{\rho(s)} \frac{\partial c^{(1)}}{\partial \theta} = - \left\{ \int_{-1}^{1} \left[\frac{2\rho(\tilde{s})\mathcal{A}(\tilde{s})\boldsymbol{R}_0 \cdot \hat{\boldsymbol{e}}_\theta(s, \theta)}{|\boldsymbol{R}_0|^3} - \frac{\rho(s)\kappa(s)\mathcal{A}(s) \sin[\theta - \theta_i(s)]}{|\tilde{s} - s|} \right] d\tilde{s} \right.$$
$$\left. + \left[\log\left(\frac{4(1 - s^2)}{\epsilon^2 \rho^2(s)} \right) - 3 \right] \rho(s)\kappa(s)\mathcal{A}(s) \sin[\theta - \theta_i(s)] \right\}, \tag{2.45}$$

where $\hat{\boldsymbol{e}}_\theta(s, \theta) = -\hat{\boldsymbol{n}}(s) \sin[\theta - \theta_i(s)] + \hat{\boldsymbol{b}}(s) \cos[\theta - \theta_i(s)]$. Using the notation $\theta_m(s, \theta) \equiv \theta - \theta_i(s)$, we can rearrange (2.45) as

$$\frac{1}{\rho(s)} \frac{\partial c^{(1)}}{\partial \theta} = +A_s(s) \sin \theta_m(s, \theta) + A_c(s) \cos \theta_m(s, \theta), \tag{2.46}$$

where

$$A_s(s) = \int_{-1}^{1} \left[\frac{\rho(\tilde{s})\mathcal{A}(\tilde{s})[\boldsymbol{R}_0 \cdot \hat{\boldsymbol{n}}(s)]}{|\boldsymbol{R}_0|^3} + \frac{\rho(s)\kappa(s)\mathcal{A}(s)}{2|\tilde{s} - s|} \right] d\tilde{s}$$
$$- \frac{1}{2} \left[\log\left(\frac{4(1 - s^2)}{\epsilon^2 \rho^2(s)} \right) - 3 \right] \rho(s)\kappa(s)\mathcal{A}(s), \tag{2.47}$$

$$A_c(s) = - \int_{-1}^{1} \frac{\rho(\tilde{s})\mathcal{A}(\tilde{s})\boldsymbol{R}_0 \cdot \hat{\boldsymbol{b}}(s)}{|\boldsymbol{R}_0|^3} d\tilde{s}. \tag{2.48}$$

Substituting (2.46) into (2.44) gives

$$
\boldsymbol{v}_{slip}(s,\theta) = \mathcal{M}(s)\left(\hat{\boldsymbol{t}}(s)\frac{\partial c^{(0)}}{\partial s} + [A_s(s)\sin\theta_m(s,\theta) + A_c(s)\cos\theta_m(s,\theta)]\right.
$$
$$
\left.\times\,[-\hat{\boldsymbol{n}}(s)\sin\theta_m(s,\theta) + \hat{\boldsymbol{b}}(s)\cos\theta_m(s,\theta)]\right), \tag{2.49}
$$

and using the double angle trigonometrical formulae we find that the slip velocity has only zero and second modes,

$$
\boldsymbol{v}_{slip}(s,\theta) = \frac{1}{2}\mathcal{M}(s)\left\{\left[2\hat{\boldsymbol{t}}(s)\frac{\partial c^{(0)}}{\partial s} - \hat{\boldsymbol{n}}(s)A_s(s) + \hat{\boldsymbol{b}}(s)A_c(s)\right]\right.
$$
$$
+\,\cos 2\theta_m(s,\theta)[+\hat{\boldsymbol{n}}(s)A_s(s) + \hat{\boldsymbol{b}}(s)A_c(s)]
$$
$$
\left.+\,\sin 2\theta_m(s,\theta)[-\hat{\boldsymbol{n}}(s)A_c(s) + \hat{\boldsymbol{b}}(s)A_s(s)]\right\}. \tag{2.50}
$$

In the case of planar filaments, $\boldsymbol{R}_0(s,\tilde{s})\cdot\hat{\boldsymbol{b}}(s)\equiv 0$ and hence $A_c = 0$. This reduces (2.50) to

$$
\boldsymbol{v}_{slip}(s,\theta) = \frac{1}{2}\mathcal{M}(s)\left(2\hat{\boldsymbol{t}}(s)\frac{\partial c^{(0)}}{\partial s} + A_s(s)[\hat{\boldsymbol{n}}(s)(\cos 2\theta_m(s,\theta) - 1) + \hat{\boldsymbol{b}}(s)\sin 2\theta_m(s,\theta)]\right). \tag{2.51}
$$

Given the activity, mobility and geometry of the filament, we can find the concentration, the concentration gradients and then the phoretic slip velocity field on the surface of the filament according to (2.50).

2.9. *Phoretic swimming kinematics*

We now turn to the problem of finding the leading-order swimming (rigid body) dynamics resulting from the slip velocity forcing defined in (2.50), namely the translational velocity $\boldsymbol{U}_{sw}$ and rotational velocity $\boldsymbol{\Omega}_{sw}$.

2.9.1. *Fourier modes of surface velocities and tractions*

Equations (2.50), (2.51) already have the correct form in order to use the Fourier mode description of surface velocity described by Koens & Lauga (2018), who decomposed the surface velocity and traction in Fourier modes

$$
2\pi\boldsymbol{U}(s,\theta) = \boldsymbol{U}_0(s) + \sum_{n=1}^{\infty}[\boldsymbol{U}_{c,n}(s)\cos n\theta_m(s,\theta) + \boldsymbol{U}_{s,n}(s)\sin n\theta_m(s,\theta)], \tag{2.52a}
$$

$$
2\pi\rho(s)\boldsymbol{f}(s,\theta) = \boldsymbol{f}_0(s) + \sum_{n=1}^{\infty}[\boldsymbol{f}_{c,n}(s)\cos n\theta_m(s,\theta) + \boldsymbol{f}_{s,n}(s)\sin n\theta_m(s,\theta)]. \tag{2.52b}
$$

We write the rigid body motion as

$$
\begin{aligned}
\boldsymbol{U}_{sw} + \boldsymbol{\Omega}_{sw}\times\boldsymbol{S}(s,\theta) &= \boldsymbol{U}_{sw} + \boldsymbol{\Omega}_{sw}\times\boldsymbol{r}(s) + \epsilon\rho(s)\boldsymbol{\Omega}_{sw}\times\hat{\boldsymbol{e}}_{\rho}(s,\theta) \\
&= \boldsymbol{U}_{sw} + \boldsymbol{\Omega}_{sw}\times\boldsymbol{r}(s) \\
&\quad + \epsilon\rho(s)\boldsymbol{\Omega}_{sw}\times\hat{\boldsymbol{n}}(s)\cos\theta_m(s,\theta) \\
&\quad + \epsilon\rho(s)\boldsymbol{\Omega}_{sw}\times\hat{\boldsymbol{b}}(s)\sin\theta_m(s,\theta).
\end{aligned} \tag{2.53}
$$

The contributions of the first sine and cosine modes of the surface velocity due to rigid body motion are $O(\epsilon)$, hence the leading-order Fourier mode decomposition of the total surface velocity (i.e. the sum of the rigid body motion and phoretic slip velocity) is

$$U_0(s) = 2\pi[U_{sw} + \boldsymbol{\Omega}_{sw} \times r(s)] + \pi\mathcal{M}(s) \left[2\hat{t}(s) \frac{\partial c^{(0)}}{\partial s} - \hat{n}(s)A_s(s) + \hat{b}(s)A_c(s) \right], \quad (2.54a)$$

$$U_{c,2}(s) = \pi\mathcal{M}(s)[+\hat{n}(s)A_s(s) + \hat{b}(s)A_c(s)], \quad (2.54b)$$

$$U_{s,2}(s) = \pi\mathcal{M}(s)[-\hat{n}(s)A_c(s) + \hat{b}(s)A_s(s)], \quad (2.54c)$$

where the rigid body kinematics $(U_{sw}, \boldsymbol{\Omega}_{sw})$ are to be found by imposing the force and torque balances on the filament. The total force and torque on the filament are

$$F_{tot} = \int_{-1}^{1} \int_{-\pi}^{\pi} f(\tilde{s}, \tilde{\theta}) \left| \frac{\partial S}{\partial \tilde{s}} \times \frac{\partial S}{\partial \tilde{\theta}} \right| d\tilde{\theta} \, d\tilde{s}, \quad (2.55a)$$

$$T_{tot} = \int_{-1}^{1} \int_{-\pi}^{\pi} S(\tilde{s}, \tilde{\theta}) \times f(\tilde{s}, \tilde{\theta}) \left| \frac{\partial S}{\partial \tilde{s}} \times \frac{\partial S}{\partial \tilde{\theta}} \right| d\tilde{\theta} \, d\tilde{s}, \quad (2.55b)$$

and substituting the surface element form given by (2.20) yields

$$F_{tot} = \int_{-1}^{1} \int_{-\pi}^{\pi} f(\tilde{s}, \tilde{\theta})\epsilon\rho(\tilde{s})[1 + O(\epsilon)] \, d\tilde{\theta} \, d\tilde{s}, \quad (2.56a)$$

$$T_{tot} = \int_{-1}^{1} \int_{-\pi}^{\pi} [r(\tilde{s}) + \epsilon\rho(\tilde{s})\hat{e}_\rho(\tilde{s}, \tilde{\theta})] \times f(\tilde{s}, \tilde{\theta})\epsilon\rho(\tilde{s})[1 + O(\epsilon)] \, d\tilde{\theta} \, d\tilde{s}. \quad (2.56b)$$

With $f(s, \theta)$ given by (2.52b), due to the periodicity of the cosine and sine modes making vanishing contributions, we see that the force and torque balances to leading order are

$$\int_{-1}^{1} f_0(\tilde{s}) \, d\tilde{s} = \mathbf{0}, \quad (2.57a)$$

$$\int_{-1}^{1} r(\tilde{s}) \times f_0(\tilde{s}) \, d\tilde{s} = \mathbf{0}. \quad (2.57b)$$

2.9.2. *Phoretic swimming kinematics from slender body theory of viscous propulsion*

After expanding the boundary integral equation for Stokes flow for a 3-D filament of arbitrary geometry, Koens & Lauga (2018) derived the following relation between the surface traction modes on the filament and the modes of the surface velocities,

$$4U_0(s) = \int_{-1}^{1} d\tilde{s} \left(\frac{1 + \hat{R}_0\hat{R}_0}{|R_0|} \cdot f_0(\tilde{s}) - \frac{1 + \hat{t}\hat{t}}{|\tilde{s} - s|} \cdot f_0(s) \right)$$

$$+ \left[\log\left(\frac{4\rho^2(s)}{\epsilon^2(1 - s^2)} \right) (1 + \hat{t}\hat{t}) + 1 - 3\hat{t}\hat{t} \right] \cdot f_0(s) + O(\epsilon), \quad (2.58a)$$

$$2nU_{c,n}(s) = (1 + \hat{t}\hat{t}) \cdot f_{c,n}(s) + O(\epsilon), \quad (n > 0) \quad (2.58b)$$

$$2nU_{s,n}(s) = (1 + \hat{t}\hat{t}) \cdot f_{s,n}(s) + O(\epsilon), \quad (n > 0). \quad (2.58c)$$

Thus in order to find the leading-order rigid body kinematics (U_{sw}, $\boldsymbol{\Omega}_{sw}$) of the filament, one must solve the following system for the unknown force per unit length $\boldsymbol{f}_0(s)$,

$$8\pi[U_{sw} + \boldsymbol{\Omega}_{sw} \times \boldsymbol{r}(s) + \boldsymbol{u}_0^{phor}(s)]$$
$$= \int_{-1}^{1} [\boldsymbol{G}(s, \tilde{s}) \cdot \boldsymbol{f}_0(\tilde{s}) - \boldsymbol{J}(s, \tilde{s}) \cdot \boldsymbol{f}_0(s)] \, d\tilde{s} + \boldsymbol{L}(s) \cdot \boldsymbol{f}_0(s), \quad (2.59)$$

where the unknowns (U_{sw}, $\boldsymbol{\Omega}_{sw}$) are such that zero net force (2.57a) and torque (2.57b) act on the swimmer, and where

$$\boldsymbol{u}_0^{phor}(s) = \frac{1}{2}\mathcal{M}(s) \left[2\hat{\boldsymbol{t}}(s)\frac{\partial c^{(0)}}{\partial s} - \hat{\boldsymbol{n}}(s)A_s(s) + \hat{\boldsymbol{b}}(s)A_c(s) \right], \quad (2.60)$$

is the average slip velocity (as in (2.50)) over θ, i.e. $\boldsymbol{u}_0^{phor}(s) = (1/2\pi) \int_{-\pi}^{\pi} \boldsymbol{v}_{slip}(s, \theta) \, d\theta$, that is the zeroth mode of the phoretic slip velocity according to the definition for modes, equation (2.54a) divided by 2π. We also have defined the tensors

$$\boldsymbol{G}(s, \tilde{s}) = \frac{\mathbf{1} + \hat{\boldsymbol{R}}_0(s, \tilde{s})\hat{\boldsymbol{R}}_0(s, \tilde{s})}{|\boldsymbol{R}_0(s, \tilde{s})|}, \quad (2.61a)$$

$$\boldsymbol{J}(s, \tilde{s}) = \frac{\mathbf{1} + \hat{\boldsymbol{t}}(s)\hat{\boldsymbol{t}}(s)}{|\tilde{s} - s|}, \quad (2.61b)$$

$$\boldsymbol{L}(s) = \log\left(\frac{4\rho^2(s)}{\epsilon^2(1 - s^2)}\right)(\mathbf{1} + \hat{\boldsymbol{t}}(s)\hat{\boldsymbol{t}}(s)) + \mathbf{1} - 3\hat{\boldsymbol{t}}(s)\hat{\boldsymbol{t}}(s), \quad (2.61c)$$

for a more compact notation. Note that $\boldsymbol{G}(s, \tilde{s}) = \boldsymbol{G}(\tilde{s}, s)$ and $\boldsymbol{J}(s, \tilde{s}) = \boldsymbol{J}(\tilde{s}, s)$.

A numerical implementation of this system of equations is given in § 3. Following a validation of our theory in §§ 4, 5, we present some simple results in §§ 6, 7.

3. Implementation of slender phoretic theory

In this section, we describe how to numerically implement SPT to find the surface concentration field and phoretic slip velocity given the activity on a filament of arbitrary shape, and then couple it with slender body theory of Koens & Lauga (2018) to find the swimming kinematics. Since the aim of this work is the theoretical development of the SPT, the following implementation is somewhat rudimentary, but will be shown to be sufficiently accurate and fast for our purposes. We note that calculating the concentration $c(s, \theta)$ with SPT amounts to merely evaluating a line integral, rather than solving an integral equation, as required for boundary element approaches.

3.1. *Numerical implementation*

The filament is first partitioned into N_{elts} segments of equal length l_{tot}/N_{elts}. The nth segment, denoted by E_n, has contour length l_n and parameterised by its contour length parameter s taking values in $(s_n - l_n/2, s_n + l_n/2)$ where s_n is the midpoint of E_n (according to contour length), which we will refer to as the nth collocation point.

We simply evaluate the concentration field on the filament surface according to (2.43), using Gaussian quadrature over each segment. When the evaluation point

lies in the element over which the integration takes place, it is sufficient to simply use a high-order even quadrature rule, so that no quadrature point lies at $\tilde{s} = s$. Although the integrand is non-singular at this point, this regularity arises from two singularities cancelling, and so for numerical purposes the point should be avoided.

Using a bicubic spline interpolant of the concentration field $c(s, \theta)$ with periodic boundary conditions in θ and clamped boundary conditions for s, we can use functional derivatives to find the partial derivatives of the concentration along s, θ, and hence evaluate the phoretic slip velocity field on the surface of the filament from (2.44).

For the kinematics, we will only need the zeroth mode of the phoretic slip velocity, $\boldsymbol{u}_0^{phor}$, at the collocation points, which we can calculate according to (2.60). For the evaluation of $\partial c^{(0)}/\partial s$, we use the functional derivative of a cubic spline data interpolation for $c^{(0)}$ based on its values at the collocation points. The coefficients A_s, A_c are evaluated from (2.47)–(2.48) using Gaussian quadrature for the definite integrals.

With the zeroth mode of the phoretic slip velocity at hand, we can now proceed to find the swimming kinematics by numerically implementing slender body theory according to Koens & Lauga (2018). The force per unit length $\boldsymbol{f}_0(s)$ along E_n is approximated as being constant on each segment, taking the value $\boldsymbol{f}_0[n]$. Then (2.57a)–(2.57b) become

$$\sum_{n=1}^{N_{elts}} l_n \boldsymbol{f}_0[n] = \boldsymbol{0}, \tag{3.1a}$$

$$\sum_{n=1}^{N_{elts}} \left(\int_{E_n} \boldsymbol{r}(\tilde{s}) \, \mathrm{d}\tilde{s} \right) \times \boldsymbol{f}_0[n] = \boldsymbol{0}. \tag{3.1b}$$

For l_n small enough, we can approximate $\boldsymbol{r}(\tilde{s})$ with $\tilde{s} \in E_n$ as

$$\boldsymbol{r}(\tilde{s}) = \boldsymbol{r}(s_n) + (\tilde{s} - s_n)\hat{\boldsymbol{t}}(s_n) + \tfrac{1}{2}(\tilde{s} - s_n)^2 \kappa(s_n)\hat{\boldsymbol{n}}(s_n) + O(l_n^3) \tag{3.2}$$

and use

$$\int_{s_n - l_n/2}^{s_n + l_n/2} (\tilde{s} - s_n)^m \, \mathrm{d}\tilde{s} = \frac{l_n^{m+1}}{2^{m+1}(m+1)}[1 - (-1)^{m+1}] \tag{3.3}$$

to obtain

$$\int_{E_n} \boldsymbol{r}(\tilde{s}) \, \mathrm{d}\tilde{s} = \boldsymbol{r}(s_n)l_n + \tfrac{1}{24}\kappa(s_n)\hat{\boldsymbol{n}}(s_n)l_n^3 + O(l_n^5). \tag{3.4}$$

We assume that all segments have equal contour lengths $l_n = l_{elt} \, \forall n$. Equations (3.1a)–(3.1b) become

$$\sum_{n=1}^{N_{elts}} \boldsymbol{f}_0[n] = \boldsymbol{0}, \tag{3.5a}$$

$$\sum_{n=1}^{N_{elts}} \left[\boldsymbol{r}(s_n) + \frac{l_{elt}^2}{24}\kappa(s_n)\hat{\boldsymbol{n}}(s_n) + O(l_{elt}^4) \right] \times \boldsymbol{f}_0[n] = \boldsymbol{0}, \tag{3.5b}$$

noting that for reasonable curvatures and small segments, the term $l_{elt}^2 \kappa(s_n)/24$ is also negligibly small. Evaluating (2.59) at the ith collocation point, s_i,

$$8\pi[\boldsymbol{U}_{sw} + \boldsymbol{\Omega}_{sw} \times \boldsymbol{r}(s_i) + \boldsymbol{u}_0^{phor}(s_i)]$$
$$= \int_{-1}^{1} [\boldsymbol{G}(s_i, \tilde{s}) \cdot \boldsymbol{f}_0(\tilde{s}) - \boldsymbol{J}(s_i, \tilde{s}) \cdot \boldsymbol{f}_0(s_i)] \, \mathrm{d}\tilde{s} + \boldsymbol{L}(s_i) \cdot \boldsymbol{f}_0(s_i). \tag{3.6}$$

For our element-based approach, we break the integral over the entire filament into a sum of integrals over the segments, in each of which $f_0(s)$ takes a constant value.

$$8\pi[U_{sw} + \Omega_{sw} \times r(s_i) + u_0^{phor}(s_i)]$$
$$= \sum_{j=1}^{N_{elts}} \int_{E_j} [G(s_i, \tilde{s}) \cdot f_0[j] - J(s_i, \tilde{s}) \cdot f_0[i]] \, \mathrm{d}\tilde{s} + L(s_i) \cdot f_0[i]. \quad (3.7)$$

We aim to obtain a system of equations of the form

$$8\pi[U_{sw} + \Omega_{sw} \times r(s_i) + u_0^{phor}(s_i)] = \sum_{j=1}^{N_{elts}} M_{ij} \cdot f_0[j], \quad (3.8)$$

and solve (3.8), (3.5a) and (3.5b) for the unknowns $\{f_0[i], i = 1, \ldots, N_{elts}\}, U_{sw}, \Omega_{sw}$. Each submatrix M_{ij} is given by

$$M_{ij} = \begin{cases} \displaystyle\int_{E_j} G(s_i, \tilde{s}) \, \mathrm{d}\tilde{s} & \text{if } i \neq j \\ \displaystyle\int_{E_i} [G(s_i, \tilde{s}) - J(s_i, \tilde{s})] \, \mathrm{d}\tilde{s} - \int_{\Omega \backslash E_i} J(s_i, \tilde{s}) \, \mathrm{d}\tilde{s} + L(s_i) & \text{if } i = j. \end{cases} \quad (3.9)$$

Note for the diagonal submatrices, M_{ij} with $i = j$, we avoid any singularities by having the difference $[G(s_i, \tilde{s}) - J(s_i, \tilde{s})]$ (which is regular over E_i as the singularities have cancelled each other) integrated over E_i, and $J(s_i)$ (which is singular in E_i) integrated over the entire filament except E_i, denoted by $\Omega \backslash E_i$. We formulate the entire system as

$$\begin{pmatrix} M_{11} & \cdots & M_{1N_{elts}} & -\mathbf{1}_{3\times3} & \epsilon \cdot r(s_1) \\ \vdots & \ddots & \vdots & \vdots & \vdots \\ M_{N_{elts}1} & \cdots & M_{N_{elts}N_{elts}} & -\mathbf{1}_{3\times3} & \epsilon \cdot r(s_{N_{elts}}) \\ \mathbf{1}_{3\times3} & \cdots & \mathbf{1}_{3\times3} & \mathbf{0}_{3\times3} & \mathbf{0}_{3\times3} \\ \epsilon \cdot r(s_1) & \cdots & \epsilon \cdot r(s_{N_{elts}}) & \mathbf{0}_{3\times3} & \mathbf{0}_{3\times3} \end{pmatrix} \begin{pmatrix} f_0[1] \\ \vdots \\ f_0[N_{elts}] \\ U_{sw} \\ \Omega_{sw} \end{pmatrix} = \begin{pmatrix} u_0^{phor}(s_1) \\ \vdots \\ u_0^{phor}(s_{N_{elts}}) \\ \mathbf{0}_{3\times1} \\ \mathbf{0}_{3\times1} \end{pmatrix},$$
$$(3.10)$$

where ϵ is the Levi-Civita tensor such that $(\epsilon \cdot r) \cdot \Omega_{sw} = r \times \Omega_{sw}$. We use the notation $\mathbf{0}_{3\times1}$ for the 3×1 zero vector, the notation $\mathbf{0}_{3\times3}$ for the 3×3 zero matrix and similarly $\mathbf{1}_{3\times3}$ for the 3×3 identity matrix. The last two block lines of the matrix on the left-hand side of (3.10) enforce force and torque balances. Note that it is also possible to calculate the swimming velocity using a version of the reciprocal theorem that is appropriate for filaments, which may be used to give more detailed insight into the total contributions of azimuthal slip flows.

3.2. *Computational cost*

Before we proceed with the method validation and results, it is worth briefly discussing the computational efficiency gains in employing SPT over the boundary element method (BEM), Montenegro-Johnson (2018) and providing some benchmarks. In doing so, we will focus on the gains in calculating the chemical solute concentration, which represents our novel contribution.

	SPT	BEM
Discretisation in s, N_s	100	100
Discretisation in θ, N_θ	20	20
Evaluation points N_{eval}	2000	2000
Quad points/element (singular)	20	190
Quad points/element (non-singular)	20	28
Geometry runtime (s)	0.014	0.26
Concentration runtime (s)	0.044	12.9

TABLE 1. An indication of the computational savings that can be made by employing SPT over the boundary element method. Simulations run on a Macbook Pro 2.9 GHz Intel Core i7 (2017) with 16 GB 2133 MHz LPDDR3 RAM.

The computational gains from employing SPT over the BEM arise in two parts of the code, (a) generating the filament geometry, in other words computational mesh and quadrature points, and (b) solving for the surface solute concentration. Once $c(s, \theta)$ at a cloud of points the surface is available, the same techniques may be used to evaluate the concentration gradient for the slip velocity, and so this process is comparable (and takes a negligible time). Similarly, once this slip velocity is available, either SBT or the BEM may be used to solve for the hydrodynamics (with SBT significantly faster). The benchmark results are given in table 1.

Simulations were performed on a 2017 Macbook Pro using Matlab. It should be noted that the code is efficient, but not precompiled. The BEM code uses Fekete quadrature over quadrilateral triangles, with a high-order rule (190 points) when integrating a triangle where the evaluation point lies on a vertex, and a lower-order rule (28 points) for other triangles. Note that while these values seem much higher than the SPT quadrature, the fact that these points are spread over two dimensions makes the high-order rule comparable, and the low-order rule significantly coarser. Calculating the slip velocity via spline interpolation took $O(0.01)$ seconds for both methods.

A key reason for this speed up is not only the reduction in the dimension of the integral equation from 2 (BEM) to 1 (SPT), but also the fact that SPT gives the surface concentration by evaluating an integral, whereas BEM requires one to solve an integral equation (which entails setting up and solving a matrix system). As a crude estimate, evaluation requires $O(N_s^2)$, whereas the solution for BEM requires $O(N_{eval}^3)$ steps ($N_{eval} \gg N_s$) to solve for a direct solver, although this could be reduced using iterative solvers such as the generalized minimal residual method (GMRES).

3.3. *Layout of validation and results*

In the following sections, we validate and apply SPT to various filament geometries, cross-sections and activity patterns of increasing complexity, as summarised in figure 2. Throughout, we set the mobility $\mathcal{M} = -1$, so that slip flows go from high surface solute concentrations to low. Firstly, straight rods are used to validate our SPT results against analytical formulae for prolate spheroids. Secondly, planar curved rods (with uniform cross-section) are validated against boundary element computations using the authors' previously published regularised singularity code (Montenegro-Johnson, Michelin & Lauga 2015; Varma, Montenegro-Johnson & Michelin 2018), paying particular attention to the important azimuthal variation. Next, planar curved rods are
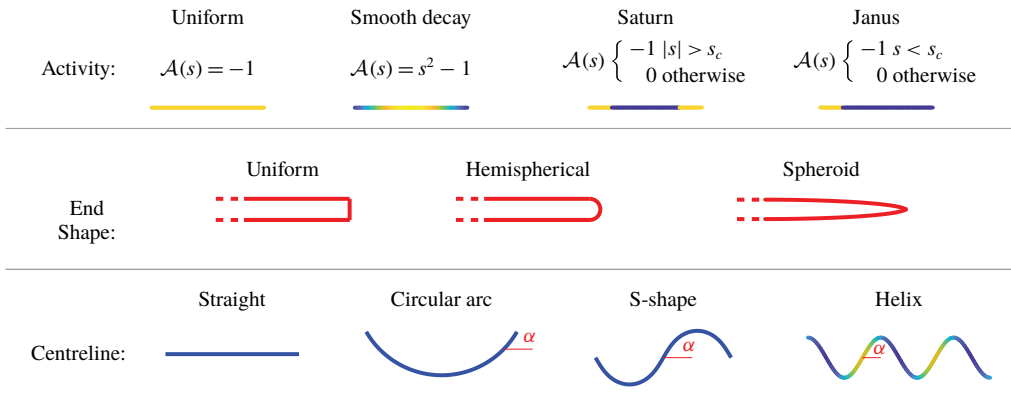
FIGURE 2. Summary of the different activity patterns (uniform $\mathcal{A}(s) = -1$, smooth decay $\mathcal{A}(s) = s^2 - 1$, Saturn – 2 symmetric active caps, Janus – 1 active cap), cross-sectional radius profiles (uniform, hemispherical cap used for BEM, prolate spheroid) and centreline geometries (straight, circular arc, S-shape, helix), used throughout the results section.

analysed with SPT – a circular arc and sinusoidal S-shaped centreline. The impact of azimuthal phoretic effects on the resulting kinematics is calculated. Finally, we consider 3-D helical phoretic filaments, focusing on the Janus helix, an autophoretic swimmer with the ability to explore space on a helical trajectory, relevant to sensing and enhanced 3-D mixing applications.

4. Validation against analytics for autophoretic prolate spheroids

We first validate our results from the numerical implementation of SPT against the analytical solution of Michelin & Lauga (2017) for straight, spheroidal particles. Michelin & Lauga (2017) used spheroidal polar coordinates and decomposed the concentration field into the associated Legendre polynomials to solve Laplace's equation for Janus prolate and oblate spheroids. Given the concentration field, the Reciprocal Theorem was then employed to find the translational kinematics, using the classical solution of Oberbeck for the stress field of translating spheroids (Lamb 1932; Happel & Brenner 1965). Figure 3(a) shows the root mean square percentage error in the surface concentration of a uniformly active prolate spheroid as calculated by SPT compared to Michelin & Lauga (2017), as a function of the slenderness parameter ϵ. We used 20-point Gaussian quadrature over 100 segments for the SPT calculation, and 801 modes of the series of the analytical solution by Michelin & Lauga (2017). The error decays like ϵ^2, as predicted by SPT: equation (2.43) shows that the leading-order expression for the concentration field is correct with $O(\epsilon^2)$ error.

Figure 3(b) shows the surface concentration along the filament, parameterised by its arclength, $-1 < s < 1$, for a set of Janus prolate spheroids with $\epsilon = 0.01$ and varying catalytic coverage. Our SPT predictions show good agreement with the solution of Michelin & Lauga (2017) (dashed black line). Note that this close agreement is in some ways slightly surprising at the edge of the Janus cap; our formulation requires that $\mathcal{A}(s)$ varies slowly across the filament surface. In practice, our result here shows that the discontinuity may be effectively handled by ensuring that the discontinuity lies at the endpoint between the segments of either side, hence the use of 100 segments.
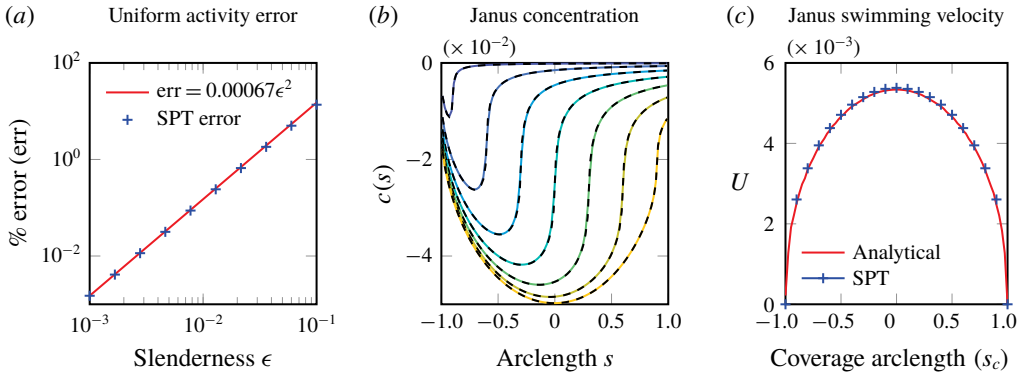
FIGURE 3. Validation of SPT versus the series solution of Michelin & Lauga (2017). (*a*) The root mean square percentage error in the surface concentration of a uniformly active prolate spheroid as calculated by SPT, as a function of the slenderness parameter ϵ. (*b*) The surface concentration as a function of arclength s of a set of 'Janus' prolate spheroids with $\epsilon = 0.01$, with active caps such that $s_c < -0.9, -0.6, \ldots, 0.9$ from dark to light respectively. The solution of Michelin and Lauga is given in each case by the dashed black line. (*c*) Comparison of the swimming velocities of Janus prolate spheroids with $\epsilon = 0.01$ as a function of s_c (−1 all inert, 1 all active).

In figure 3(*c*) we plot the swimming velocity of a slender ($\epsilon = 0.01$) Janus prolate spheroid as a function of the catalytic cap coverage s_c (−1 all inert, 1 all active) as calculated by SPT versus the solution of Michelin & Lauga (2017), showing further good agreement. The spheroid swims with the inert side at the front, i.e. to the right in figure 2.

5. Validation against BEM: planar filaments with uniform end shape

We now validate the $O(\epsilon)$ calculation of SPT by comparing against boundary element method simulations. For slender body theory (Koens & Lauga 2018), the natural choice of cross-sectional radius profile in SPT is that of a prolate spheroid. However, slender spheroidal ends are difficult to handle with regularised boundary element methods that include the double-layer term. This is because the support of the regularised singularity in the domain depends on local surface curvature (Varma *et al.* 2018), and local surface curvature diverges near the tips of the filaments in the slender limit.

Thus, in order to validate SPT for curved rods against boundary element simulations, we consider a uniform radius profile $\rho(s) = 1$ for SPT, with hemispherical end caps for the BEM (see figure 2). However, for the uniform cross-section, the logarithmic term in SPT diverges at either end. To avoid this divergence, we thus validate against the quadratic activity profile $\mathcal{A}(s) = s^2 - 1$.

The centreline of a planar filament is uniquely defined by specifying the local angle $\psi(s)$ between the tangent $\hat{t}(s)$ to the centreline and a fixed direction (here the x-axis). Then the shape of the curve can be constructed using the function $\psi(s)$ through integration, $x(s) = \int \cos(\psi(\tilde{s})) \, \mathrm{d}\tilde{s}$, and $y(s) = \int \sin(\psi(\tilde{s})) \, \mathrm{d}\tilde{s}$. Following the non-dimensionalisation in the previous sections, we parametrise the centreline by the contour length parameter s, such that $-1 < s < 1$. Circular arcs of varying curvature are parameterised such that $\psi(s) = s\alpha$, where α is equal to the curvature κ. S-shaped filaments are parameterised by a sinusoidal tangent angle $\psi(s) = \alpha \cos(\pi s)$, which
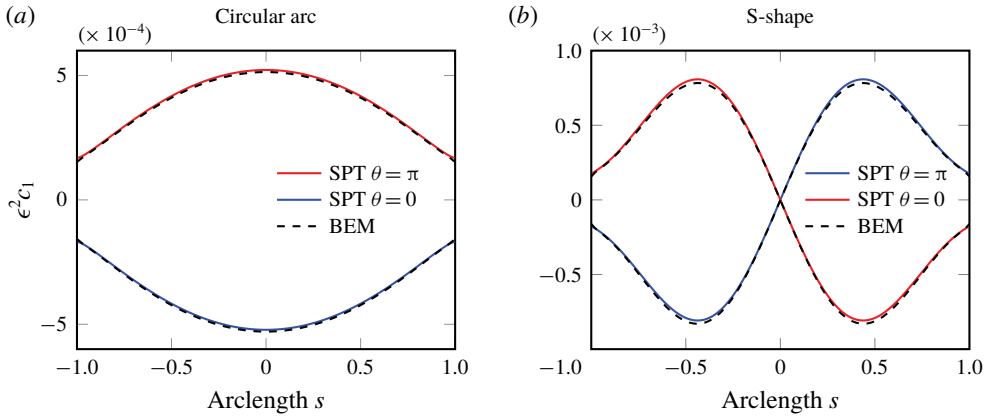
FIGURE 4. Validation of the first-order concentration correction c_1 of SPT versus boundary element simulation using a regularised singularity approach (Montenegro-Johnson *et al.* 2015) with $\mathcal{A}(s) = s^2 - 1$ for (*a*) a U-shaped filament with $\alpha = \pi/2$ and (*b*) an S-shaped filament with $\alpha = \pi/3$, showing good agreement.

gives the smooth curvature $\kappa(s) = -\alpha\pi\sin(\pi s)$. For both curves, the limiting case of $\alpha \to 0$ corresponds to a straight filament.

Since the concentration for a slender filament scales with the slenderness, azimuthal variations in the filament concentration are in fact $O(\epsilon^2)$, when the more common nondimensionalisation with respect to length is used. As such, we require a very refined boundary element mesh in order to capture this variation accurately. For accurate implementations of SPT and BEM, we can therefore expect a difference between our BEM/SPT calculations of at least $O(\epsilon^3)$, arising from the truncation of SPT. In practice, at this very small order for slender filaments, other numerical errors begin to affect the BEM solution.

With this caveat in mind, we plot the azimuthal variation in the concentration as a function of arclength for the circular arc and S-shapes in figure 4. For the case of (a) a circular arc with $\alpha = \pi/2$ (i.e. a semicircle) and (b) an S-shaped centreline with $\alpha = \pi/3$, we find good agreement between the SPT and boundary element calculations. We show the variation of $\epsilon^2 c_1$ with s at the azimuthal positions $\theta = 0$ and $\theta = \pi$, as these bound the values of $\epsilon^2 c_1$ for the rest azimuthal positions by symmetry.

We now validate the gradients of this concentration field (figure 5), which provide the phoretic slip velocity according to (2.44). Figure 5(*a*) shows $\partial c/\partial s$ for the case of a circular arc filament of uniform activity, showing the expected divergence in the gradient when calculated with SPT at the ends of the filament due to the divergence of the logarithmic term in the concentration field for uniform cross-sections. However, there is otherwise generally good agreement with the BEM, except in this small region around $s = \pm 1$. This discrepancy is removed (as expected) by taking the quadratic activity profile $\mathcal{A}(s) = s^2 - 1$. Furthermore, figure 5(*c*) shows that our SPT captures the azimuthal gradients in the concentration profile with good accuracy, which is crucial for accurate kinematics calculations.

Finally, we compare the translational and rotational velocities of circular arc and S-shape filaments as a function of the angle amplitude α (a proxy for curvature). The geometry is as shown in figure 2, where a positive translational velocity for the circular arc means swimming upwards, and a positive angular velocity for the S-shape means anticlockwise rotation about the centroid.
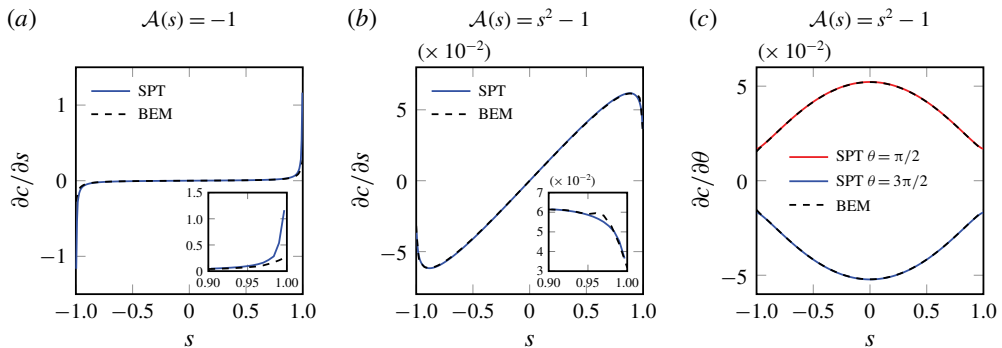
FIGURE 5. Validating concentration gradients against boundary element simulation, for a semicircular rod of constant radius (required for BEM). (*a*) For uniform activity, the slip velocity along $\theta = \pi/2$ diverges at the ends when calculated via SPT, due to the logarithmic term. (*b*) This divergence may be regularised by ensuring the activity smoothly decays to zero at either end. (*c*) Azimuthal slip flows show good agreement between SPT and BEM.

Since we have non-vanishing slip velocity at $s = \pm 1$, the (hydrodynamic) slender body theory solution also diverges at either end. However, since this is over a very small region, the swimming velocity (which can be thought of as arising from an integral of the surface slip) is not greatly impacted by this divergence. Figure 6 shows that the SPT kinematics calculations agree well with the full boundary element simulations. In particular, we note that the kinematics are changed at leading order when azimuthal slip flows are neglected (i.e. $A_s = A_c = 0$ in (2.60)), and that SPT captures this effect. Having validated our SPT against analytical and Boundary Element calculations, we now proceed with using SPT to study curved filaments with activity profiles that are more relevant to fabrication.

6. Curved planar filaments and azimuthal effects

6.1. *Azimuthal variation of the concentration field*

We now use SPT to examine the physics of slender autophoretic filaments of curved centreline. Throughout this section we consider a spheroidal end shape to ensure the regularity of the SPT formulation. Figure 7 shows colour maps of the concentration field (lines of same colour indicate the contours of the concentration field) at different arclength values (s) and azimuthal (θ) positions for the three shapes (straight *a*, circular arc *b* and S-shaped *c*) in the case of a uniform catalytic coating, $\mathcal{A}(s) = -1$, that depletes its surrounding solute.

For the straight filament (figure 7*a*), we see axisymmetry (i.e. no variation of colour with different θ at a given s) in the concentration field, as expected. We note that for the straight filament the first-order concentration field vanishes, hence figure 7(*a*) shows the zeroth-order concentration field which is axisymmetric, but non-uniform in s due to the non-local and endpoint effects already present in (2.39). For example, the closer to the endpoints, the more space there is available for diffusion, hence the solute depletion is less and the solute reactant is at a higher concentration.

For circular arc filaments, (figure 7*b*), we see a minimum of the concentration field occurring at $s = 0$ and $\theta = 0(2\pi)$, i.e. the part of the surface that is facing the centre of the semicircular centreline. This is a confinement effect arising from the curvature
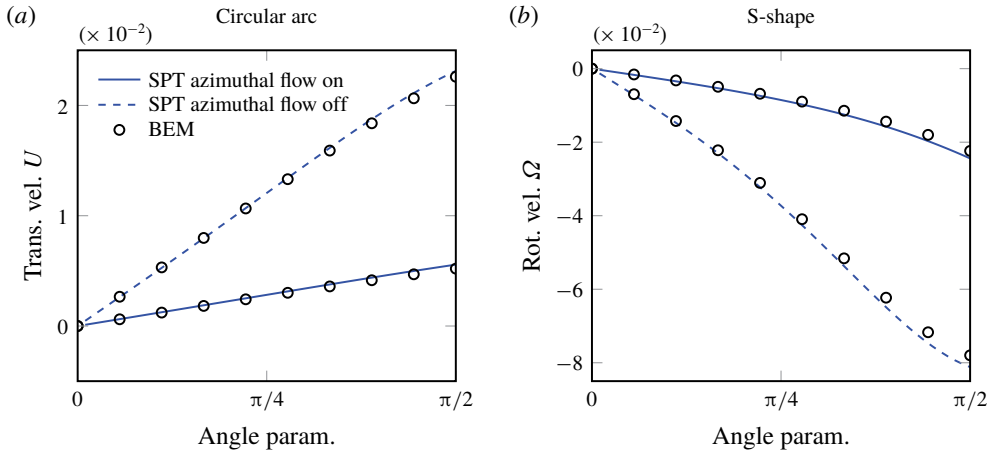
FIGURE 6. Validation of the swimming kinematics of a series of circular arcs and S-shapes as a function of the angle parameter α, with $\mathcal{A}(s) = s^2 - 1$ showing good agreement between SPT and BEM. Results obtained using the full slip flows (azimuthal and longitudinal, solid) are compared to those obtained when neglecting azimuthal slip flow ($A_s = A_c = 0$ in (2.60), dashed).
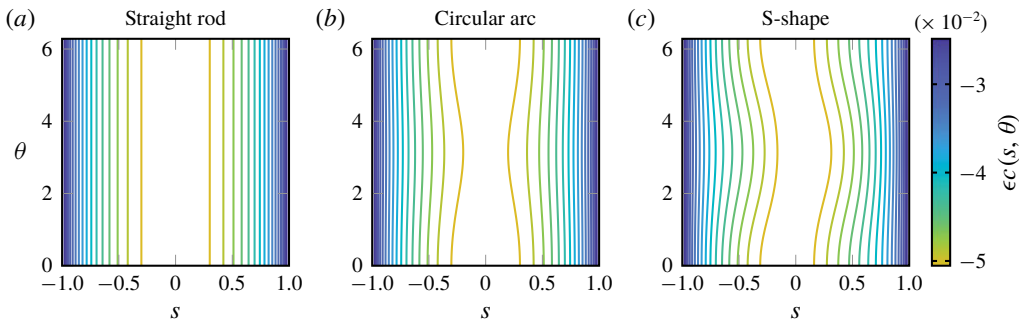

FIGURE 7. The surface concentration of uniformly active phoretic filaments with a prolate spheroidal end shape and planar centrelines with (*a*) straight shape which is stationary but pumps fluid, (*b*) circular arc shape which translates and (*c*) S-shape which rotates. Small azimuthal variation due to non-local interactions and confinement effects from curvature are visible in the circular arc and S-shaped examples.

of the centreline, as this inner part of the surface experiences more depletion of the solute from the local surface and the adjacent active parts of the surface. Close to the outer part of the surface, there is more space (due to curvature) for diffusion of solute from the bulk to the filament surface thus the solute that has been depleted due to the reaction can be replenished more easily. Straight and circular arc filament centreline shapes share the symmetry $c(s, \theta) = c(-s, \theta)$ for the concentration field, arising naturally from the centreline symmetry in $s \to -s$. This symmetry is broken by S-shaped filaments, for which $c(s, \theta) = c(-s, -\theta)$, as in figure 7(*c*). At $s = 0$, the concentration is minimised by the azimuthal positions $\theta = 0, \pi$ with $c(0, 0) = c(0, \pi)$, as these lie on the x, y plane and therefore are closer to the nearby active surfaces (by the same amount by symmetry), and $c(0, \pi/2) = c(0, 3\pi/2)$.
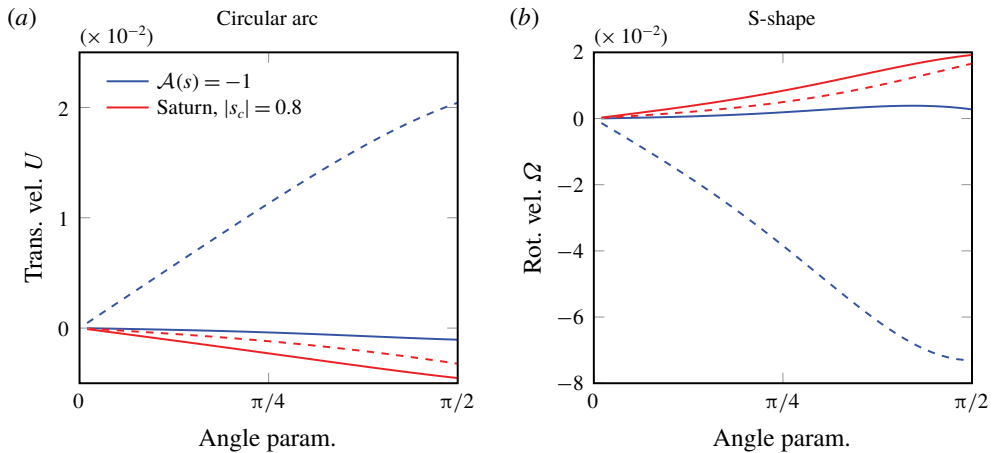
FIGURE 8. Leading-order contribution of azimuthal effects to kinematics arising from curvature and confinement. Kinematics of (*a*) circular arc and (*b*) S-shaped filaments versus the angle parameter based on SPT, for uniform and Saturn activity patterns, where the Saturn particle has two active end caps and an inert midpiece (see figure 2). Here, $\epsilon = 0.01$. Solid lines include azimuthal slip flows, dashed lines have this contribution removed, i.e. $A_s = A_c = 0$ in (2.60).

6.2. *Kinematics: leading-order contribution of azimuthal variations of the concentration field*

Turning now to the kinematics of these filaments, figure 8 shows the translational and rotational speeds for circular arc and S-shaped filaments when the azimuthal terms are included ('on' – solid lines) versus neglected ('off' – dashed), for two different activity profiles. The azimuthal effect contribution to the kinematics vanishes as α decreases to 0 in all the plots of figure 8, as expected for straight filaments that have zero curvature ($\alpha = 0$) and an axisymmetric concentration field. As α increases, so does the curvature, and hence the azimuthal effects too.

The importance of the azimuthal effects, as noted in Montenegro-Johnson (2018), is quite profound in the case of uniform activity, where neglecting their contribution results in an incorrect prediction in the direction of motion, as shown by the dashed lines in figure 8(*a*,*b*). In order to understand this, let us consider the uniformly active, circular arc filament (see also the qualitative schematic figure 9*b*). If we discount azimuthal effects, the higher solute concentration at the ends drives a longitudinal surface slip flow to the middle, giving rise to translation in the opposite direction, hence the positive velocity shown by the dashed blue line in figure 8(*a*).

Since the filament consumes solute, confinement effects mean that there is a lower surface concentration in the inner filament surface that faces the centre of the circular arc centreline. This drives an azimuthal tangential surface slip flow from the outer to the inner side of the curve. This means that, locally, the filament is acting as a 2-D squirmer (Blake 1971), with symmetry about $\theta = 0$, π. This outer to inner flow locally exerts a flow forcing towards the outer side of the cylinder, propelling the filament in that direction. This forcing is in the opposite direction to that arising from longitudinal concentration gradient, and this contribution is large enough that the overall translational velocity has a negative sign, as shown by the solid blue line in figure 8(*a*).
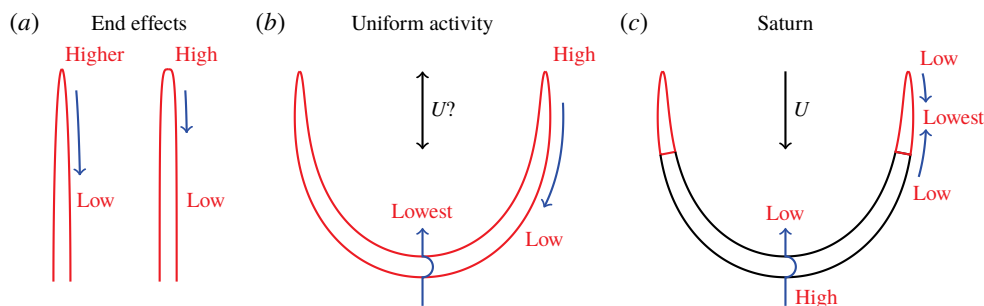
FIGURE 9. Qualitative schematic: understanding end shape and azimuthal effects. Red text indicates the relative concentration of solute in each figure, with slip flow (blue) moving from higher to lower concentrations, assuming constant, negative mobility. (*a*) The shape of the filaments affects the geometric confinement at the ends, resulting in different strength of slip flows. (*b*) A uniformly active prolate spheroid. For our parameter choices, azimuthal flows work in opposition to axial flows and hence the swimming direction is sensitive to which effect is stronger, which in turn depends on geometry and end shape. (*c*) In a capped filament azimuthal flows and axial flows work together, however, there is an opposing end-effect flow (as with the Janus prolate spheroid) that slows the swimmer.

For Saturn particles, which have two active caps and an inert midpiece (see figure 2), the active caps ensure that the tangential concentration gradients dominate (due to the fast velocity at the change in activity) and hence the kinematics with the azimuthal terms on/off have the same directionality. In more detail (see also the qualitative schematic figure 9*c*), let us consider with the case of two catalytic caps of length $\Delta s = 0.2$. The catalytic end caps in the regions $|s| > 0.8$ give rise to a lower concentration of solute at the end region, compared to the region $|s| < 0.8$, driving a slip flow across the interface at $s = 0.8$ directed from the high to the low solute concentration region (i.e. towards the ends). There is of course a small region of higher solute concentration at the very ends due to the end confinement effect (magnified by the presence of the prolate spheroidal ends – see the qualitative schematic figure 9*a*), driving a small slip flow at the very ends directed to the middle, but overall the slip flow at the interface at $|s| = 0.8$ dominates, leading to motion of the filament in the negative direction, as shown by the red, dashed line in figure 8(*a*).

Now consider the azimuthal effect, focusing on the middle region around $s = 0$, which by the confinement effect, has higher solute concentration close to the 'outer' surface that looks away from the centre of the semicircle. This drives an azimuthal flow around the filament towards the centre of the semicircle, which contributes to a negative direction, i.e. in the same direction as the kinematics with the azimuthal effects switched 'off', hence the overall speed is increased when the azimuthal effects are included, as shown by the red, solid line in figure 8(*a*).

Similar explanations hold for the kinematics of S-shaped filaments shown in figure 8(*b*).

7. Janus helix

Finally, we apply SPT to fully 3-D geometries, focusing specifically on helical centrelines. As we will see in § 7.2, Janus helical filaments give rise to helical trajectories, which offer novel exploration of space capabilities which are not currently accessible to phoretic microswimmer designs of Janus spheres, rods and prolate spheroids.
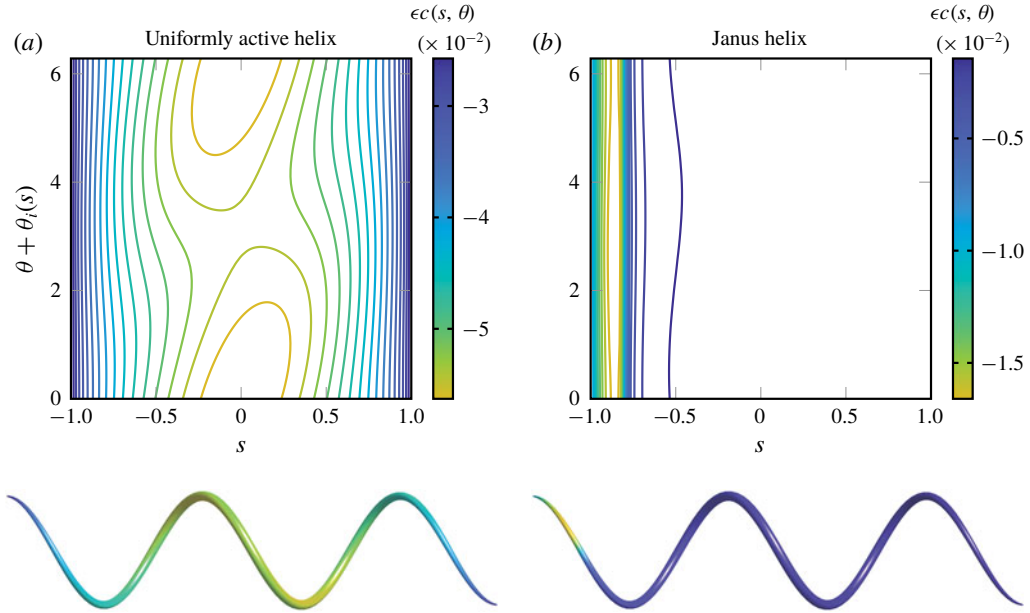
FIGURE 10. The surface concentration of (*a*) a uniformly active helix and (*b*) a Janus helix, as calculated with SPT, with $\epsilon = 0.01$, $\alpha = \pi/3$, $s_c = -0.8$ and 2.5 turns.

7.1. *Helix geometry, concentration and kinematics*

We consider a helical centreline with chirality h (taking the values ± 1 for right-handed and left-handed helices respectively), helical angle α and n turns,

$$(x, y, z) = \left(R \cos \frac{(s+1)\sin\alpha}{R}, hR \sin \frac{(s+1)\sin\alpha}{R}, s \cos\alpha \right), \tag{7.1}$$

where the helical radius R, curvature κ and torsion τ are given by

$$R = \frac{\sin\alpha}{n\pi}, \quad \kappa = \frac{\sin^2\alpha}{R}, \quad \tau = h\frac{\sin\alpha\cos\alpha}{R}, \tag{7.2a--c}$$

and its pitch by $(2\cos\alpha)/n$. We begin by validating a constant cross-section rod against BEM for a helix with 2.5 turns and $\alpha = \pi/3$, with regularised activity $\mathcal{A}(s) = -(s+1)(1 - \tanh(2s))$ and mobility $\mathcal{M} = -(s+1)(1 - \tanh(4s))$. This regularisation is somewhat similar to a single capped end, but with a smoothly decaying velocity. We achieve approximately 1 % error in the concentration field, and 2 % and 7 % errors in translational and angular velocities respectively, where angular velocity is calculated about the helix centroid. We note that this larger relative error in the swimming velocity arises from the fact that this regularised case only swims relatively slowly.

Continuing with SPT for a filament with prolate spheroidal ends, the surface concentration of a uniformly active helix is shown in figure 10(*a*) for varying arclengths (s) and azimuthal positions, using $\theta + \theta_i(s)$ in order to ensure that θ lies in $[0, 2\pi)$ (recall that by definition, $\theta_i(s)$ follows the torsion of the filament – (2.8)). The apparent shear about $\theta(s) = \pi$ is a result of this choice for $\theta_i(s)$. In figure 10(*b*), we show the surface concentration of a Janus helix capped for $s \leqslant -0.8$, with $\epsilon = 0.01$, showing strong local gradients around the capped end.
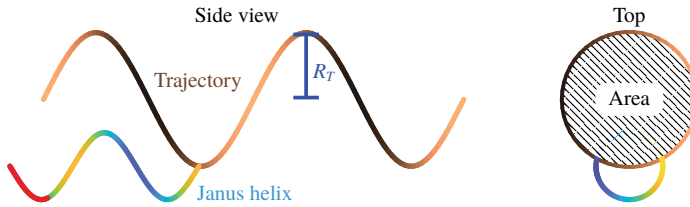
FIGURE 11. Schematic showing a Janus helix, on a helical trajectory of radius R_T, from a side and top view, demonstrating the 'exploratory area' of the swimmer πR_T^2.

7.2. *Exploration of space*

Many microswimmers make use of helical trajectories for exploring their environment and sensing, and thus also perform chemotaxis towards food resources. Helical trajectories could offer enhanced sensing and 3-D mixing to artificial phoretic microswimmer applications.

As shown schematically in figure 11, Janus helices can explore space on a helical trajectory, with radius and pitch that vary with the geometry of the helical filament. Figure 12(*a*) shows the trajectories of Janus helices of the same arclength (2), helical angle ($\pi/3$) and length of catalytic cap ($s_c = -0.9$), but different number of turns. All simulations run over the same time interval ($t = 30$ in dimensionless units). In real space, the axis of the trajectories is aligned with the $\boldsymbol{\Omega}$ vector. In figure 12(*a*) the trajectories have been rotated to be aligned vertically for the purpose of comparison. In order to quantify the ability of the different Janus helices to explore space, in figure 12(*b*) we plot the explorative area of the helical trajectory, which is equal to πR_T^2 for R_T the helix radius as in figure 11. Figure 12(*c*) shows the velocity along the axis of each helical trajectory versus the number of turns.

These plots show interesting nonlinear behaviour, with a number of transition points, the most dramatic of which is close to when the number of turns n increases above a single full turn. There are two limiting behaviours. Firstly, as $n \to 0$, the helix tends to a straight rod, and the axial velocity in turn tends to that of a straight rod. However, the explorative area does not seem to approach zero in this limit – rather the nearly straight helix may explore a non-zero or even infinite area, but take an infinite time to do it as $n \to 0$. On the other hand, as $n \to \infty$, the helix again approaches a straight rod, and we would expect the axial velocity to once more tend to the straight case. However, we cannot analyse this limit within our framework, as it entails divergent curvature κ; our analysis remains valid provided $\kappa = n\pi \sin \alpha \ll 1/\epsilon$.

We note that between these limits, we expect a decrease in axial velocity (since propulsion force does not lie solely along the axial direction), and hence we expect a minimum in axial velocity – obtained somewhere in $n \in (0.75, 1)$ for the particular values of parameters we have chosen here. This behaviour is not monotonic, but displays periodic fluctuations that change depending on whether the helix has an odd or even number of turns, that are not clearly visible in figure 12(*a*). Finally, we note that smart, stimulus-responsive materials, such as thermoresponsive hydrogel composites, could assist in exploiting both features by changing the number of turns of a Janus helix, as can occur naturally in the polymorphism of bacterial flagella (Spagnolie & Lauga 2011), so that it can have a slow, explorative mode with less than one turn, and a faster, close to straight swimming mode at higher number of turns.
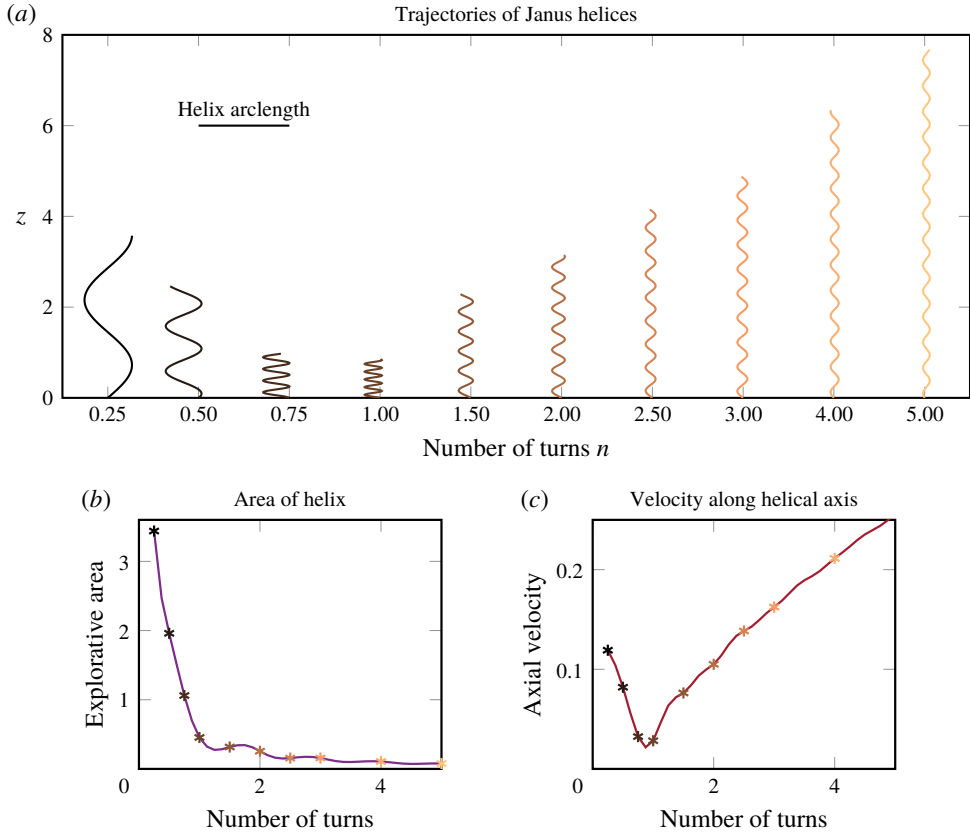
FIGURE 12. Trajectories of helical filaments with one catalytic end of length 0.1, i.e. $s_c = -0.9$, helical angle $\pi/3$ and varying number of turns. (*a*) The different helical trajectories arising from varying the number of turns. All simulations run over the same time interval ($t = 30$ in dimensionless units). The axis of the trajectories is aligned with the $\boldsymbol{\Omega}$ vector in real space. The trajectories have been rotated to be aligned vertically for the purposes of this plot. (*b*) Area of helical trajectories, i.e. πR_T^2 for helical radius R_T, versus number of turns of the Janus helix. (*c*) Velocity along the axis of each helical trajectory versus number of turns of the Janus helix.

8. Discussion

This paper provides a novel and complete framework to analyse the dynamics of slender (auto)-phoretic filaments with centrelines that are not limited to straight geometries, but are fully three-dimensional. These (auto)-phoretic filaments self-propel by catalysing a reaction of a solvent in their surroundings. Catalytic patterning on the filament surface induces differential surface reaction, which generates solute concentration gradients that drive a propulsive surface slip flow.

Previous analytical theories have considered straight slender phoretic filaments (Yariv 2008; Schnitzer & Yariv 2015; Yariv 2019). We developed a slender phoretic theory which addresses slender phoretic filaments of arbitrary shape. We used matched asymptotics to expand the boundary integral representation of the solution of the diffusion equation in the slender limit, similarly to the approach of Koens & Lauga (2018) for filaments moving in viscous fluids. In contrast to many other slender body theories, which finish at leading order, the form of the azimuthal slip flow,

necessitates that SPT be derived to first order in the slenderness of the filament. These first-order azimuthal variations to the concentration arise from confinement effects from curvature, drive azimuthal slip flows and make a leading-order contribution to the kinematics. The latter can be as profound as reversing the direction of motion.

SPT is more computationally efficient than BEM. However, although the speed up in calculating the surface concentration distribution is considerable ($\approx 300\times$), for the examples we considered herein, the boundary element calculation is not prohibitively slow at $O(10)$ s. As with classical slender body theory for Stokes flows, which has proven to be efficient and popular in the study of many biological flows, such as ciliary flows, the full capability of SPT lies in two possible extensions to the theory, that we believe will make fruitful avenues of future research. The first is in efficiently evaluating the solute dynamics of multiple filaments. This would likely use a representation of neighbouring curved filaments by line distributions of sources and dipoles, weighted by activity and curvature, but will require significant work to rigorously derive. The second use is in dynamic fluid–structure interaction problems for flexible chemically active filaments. There have been a number of recent advances in efficient simulation elastohydrodynamics combining local drag theory or slender body theory for Stokes flow with elastic beam theory (Moreau, Giraldi & Gadêlha 2018; Hall-McNair *et al.* 2019; Schoeller *et al.* 2019; Walker *et al.* 2019). Taking Hall-McNair *et al.* (2019) as an example, a typical simulation took 0.0007 s per time step, with a single beat of the active filament model (the minimum for interesting dynamics) taking approximately 20 s to resolve, i.e. around 30 000 time steps. To consider similar chemoelastohydrodynamic simulations, coupling the concentration solution via SPT would increase the total run time to approximately 22 min, whereas coupling via the boundary element method would increase the total run time to 100 h. It is also worth noting that our SPT code has as yet not been optimised for speed, and in fact more efficient implementations will certainly be able to reduce this further.

Furthermore, the form of the SPT integral equation reveals the underlying structure of the various contributions to the concentration field (and swimming velocity), providing opportunities for new insights. In particular, we note that the torsion is absent from the SPT equation, as it appears only at $O(\epsilon^2)$. The natural decomposition of the azimuthal slip flow into Fourier modes furthermore makes the theory ideal for coupling with the viscous flow slender body theory of Koens & Lauga (2018), providing further gains in efficiency. We hope that this new theory will provide the basis for researchers to begin to look at complex, interacting, flexible phoretic filament flows in three dimensions.

Acknowledgements

Declaration of interests

The authors report no conflict of interest.

Appendix A. Expansion of the kernels

A.1. *Outer region*

Expanding in the outer region, $s - \tilde{s} = O(1)$, (i.e. $\boldsymbol{R}_0(s, \tilde{s}) = O(1)$ and we can approximate $\boldsymbol{R} \approx \boldsymbol{R}_0$), and using (2.23), (2.24). Expanding $1/|\boldsymbol{R}|$,

$$
\begin{aligned}
\frac{1}{|\boldsymbol{R}|} &= [|\boldsymbol{R}_0|^2 + 2\epsilon \boldsymbol{R}_0 \cdot \boldsymbol{\mathcal{D}}_{(\tilde{s},\tilde{\theta})}^{(s,\theta)} + O(\epsilon^2)]^{-1/2} \\
&= \frac{1}{|\boldsymbol{R}_0|} \left[1 - \epsilon \frac{\boldsymbol{R}_0}{|\boldsymbol{R}_0|^2} \cdot \boldsymbol{\mathcal{D}}_{(\tilde{s},\tilde{\theta})}^{(s,\theta)} + O(\epsilon^2) \right],
\end{aligned}
\tag{A 1}
$$

which gives the outer expansions $K_1^{(o)}$, $K_2^{(o)}$ of the kernels K_1, K_2, defined in (2.22a)–(2.22b), as

$$
\begin{aligned}
K_1^{(o)} &= \frac{\rho(\tilde{s})\mathcal{A}(\tilde{s}, \tilde{\theta})}{|\boldsymbol{R}_0(s, \tilde{s})|} \left[1 - \epsilon \frac{\boldsymbol{R}_0 \cdot \boldsymbol{\mathcal{D}}_{(\tilde{s},\tilde{\theta})}^{(s,\theta)}}{|\boldsymbol{R}_0|^2} + O(\epsilon^2) \right] [1 - \epsilon \rho(\tilde{s})\kappa(\tilde{s}) \cos \theta_m(\tilde{s}, \tilde{\theta}) + O(\epsilon^2)] \\
&= \frac{\rho(\tilde{s})\mathcal{A}(\tilde{s}, \tilde{\theta})}{|\boldsymbol{R}_0(s, \tilde{s})|} \left[1 - \epsilon \left[\rho(\tilde{s})\kappa(\tilde{s}) \cos \theta_m(\tilde{s}, \tilde{\theta}) + \frac{\boldsymbol{R}_0 \cdot \boldsymbol{\mathcal{D}}_{(\tilde{s},\tilde{\theta})}^{(s,\theta)}}{|\boldsymbol{R}_0|^2} \right] + O(\epsilon^2) \right],
\end{aligned}
\tag{A 2}
$$

$$
\begin{aligned}
K_2^{(o)} &= \frac{\epsilon \rho(\tilde{s})c(\tilde{s}, \tilde{\theta})}{|\boldsymbol{R}_0|^3} \left[1 - \frac{3\epsilon \boldsymbol{R}_0 \cdot \boldsymbol{\mathcal{D}}_{(\tilde{s},\tilde{\theta})}^{(s,\theta)}}{|\boldsymbol{R}_0|^2} \right] [\boldsymbol{R}_0 + \epsilon \boldsymbol{\mathcal{D}}_{(\tilde{s},\tilde{\theta})}^{(s,\theta)}] \\
&\quad \cdot \left[\hat{\boldsymbol{e}}_\rho(\tilde{s}, \tilde{\theta}) - \epsilon \frac{\mathrm{d}\rho(\tilde{s})}{\mathrm{d}\tilde{s}} \hat{\boldsymbol{t}}(\tilde{s}) - \epsilon \rho(\tilde{s})\kappa(\tilde{s}) \cos \theta_m(\tilde{s}, \tilde{\theta}) \hat{\boldsymbol{e}}_\rho(\tilde{s}, \tilde{\theta}) \right] + O(\epsilon^3) \\
&= \epsilon \frac{\rho(\tilde{s})c(\tilde{s}, \tilde{\theta})}{|\boldsymbol{R}_0|^3} \left\{ \boldsymbol{R}_0 \cdot \hat{\boldsymbol{e}}_\rho(\tilde{s}, \tilde{\theta}) + \epsilon \left(\boldsymbol{\mathcal{D}}_{(\tilde{s},\tilde{\theta})}^{(s,\theta)} \right) \cdot \hat{\boldsymbol{e}}_\rho(\tilde{s}, \tilde{\theta}) \right. \\
&\quad - \epsilon \boldsymbol{R}_0 \cdot \left[\frac{\mathrm{d}\rho(\tilde{s})}{\mathrm{d}\tilde{s}} \hat{\boldsymbol{t}}(\tilde{s}) + \rho(\tilde{s})\kappa(\tilde{s}) \cos \theta_m(\tilde{s}, \tilde{\theta}) \hat{\boldsymbol{e}}_\rho(\tilde{s}, \tilde{\theta}) \right] \\
&\quad \left. - \epsilon (\boldsymbol{R}_0 \cdot \hat{\boldsymbol{e}}_\rho(\tilde{s}, \tilde{\theta})) \frac{3\boldsymbol{R}_0 \cdot \boldsymbol{\mathcal{D}}_{(\tilde{s},\tilde{\theta})}^{(s,\theta)}}{|\boldsymbol{R}_0|^2} + O(\epsilon^2) \right\}.
\end{aligned}
\tag{A 3}
$$

In the above expressions we keep the first two orders to ensure all relevant contributions are accounted for, in particular in anticipation of the matching to follow (A 3).

A.2. *Inner region*

A.2.1. *Inner region expansion*

In the inner region, $s - \tilde{s} = O(\epsilon)$ and we let $\tilde{s} = s + \epsilon \chi$, where χ is $O(1)$. We proceed by Taylor expanding functions of $\tilde{s}$ around s, using the Serret–Frenet equation $\partial \hat{\boldsymbol{t}}/\partial s = \kappa \hat{\boldsymbol{n}}(s)$, and from (2.9), $\partial \hat{\boldsymbol{e}}_\rho/\partial s = -\kappa(s) \cos \theta_m(s, \theta) \hat{\boldsymbol{t}}(s)$,

$$
\rho(\tilde{s}) = \rho(s) + \epsilon \chi \frac{\mathrm{d}\rho(s)}{\mathrm{d}s} + O(\epsilon^2),
\tag{A 4a}
$$

$$
\boldsymbol{r}(\tilde{s}) = \boldsymbol{r}(s) + \epsilon \chi \hat{\boldsymbol{t}}(s) + \tfrac{1}{2}(\epsilon \chi)^2 \kappa(s) \hat{\boldsymbol{n}}(s) + O(\epsilon^3),
\tag{A 4b}
$$

$$
\hat{\boldsymbol{e}}_\rho(\tilde{s}, \tilde{\theta}) = \hat{\boldsymbol{e}}_\rho(s, \tilde{\theta}) - \epsilon \chi \kappa(s) \cos \theta_m(s, \tilde{\theta}) \hat{\boldsymbol{t}}(s),
\tag{A 4c}
$$

$$S(\tilde{s}, \tilde{\theta}) = r(s) + \epsilon[\chi\hat{t}(s) + \rho(s)\hat{e}_\rho(s, \tilde{\theta})]$$
$$+ \epsilon^2\left[\frac{1}{2}\chi^2\kappa(s)\hat{n}(s) + \chi\frac{d\rho(s)}{ds}\hat{e}_\rho(s, \tilde{\theta}) - \rho(s)\chi\kappa(s)\cos\theta_m(s, \tilde{\theta})\hat{t}(s)\right]$$
$$+ O(\epsilon^3). \tag{A 4d}$$

Equation (2.17) gives

$$R = \epsilon[\hat{R}_{(i)}^{(1)} + \epsilon\hat{R}_{(i)}^{(2)}] + O(\epsilon^3), \tag{A 5}$$

where

$$\hat{R}_{(i)}^{(1)} = -\chi\hat{t}(s) + \rho(s)[\hat{e}_\rho(s, \theta) - \hat{e}_\rho(s, \tilde{\theta})], \tag{A 6a}$$

$$\hat{R}_{(i)}^{(2)} = -\left[\frac{1}{2}\chi^2\kappa\hat{n}(s) + \chi\frac{d\rho(s)}{ds}\hat{e}_\rho(s, \tilde{\theta}) - \chi\rho(s)\kappa(s)\cos\theta_m(s, \tilde{\theta})\hat{t}(s)\right], \tag{A 6b}$$

$$|\hat{R}_{(i)}^{(1)} + \epsilon\hat{R}_{(i)}^{(2)}| = |\hat{R}_{(i)}^{(1)}|[1 + \epsilon\hat{R}_{(i)}^{(1)} \cdot \hat{R}_{(i)}^{(2)}/|\hat{R}_{(i)}^{(1)}|^2 + O(\epsilon^2)]. \tag{A 6c}$$

Using these, the inner expansions of K_1, K_2 become

$$\epsilon|\hat{R}_{(i)}^{(1)}|K_1^{(i)} = \rho(s)\mathcal{A}(s, \tilde{\theta}) + \epsilon\left(+\chi\left[\rho(s)\partial_s\mathcal{A}(s, \tilde{\theta}) + \frac{d\rho(s)}{ds}\mathcal{A}(s, \tilde{\theta})\right]\right.$$
$$\left. - \rho(s)\mathcal{A}(s, \tilde{\theta})[\rho(s)\kappa(s)\cos\theta_m(s, \tilde{\theta}) + \hat{R}_{(i)}^{(1)} \cdot \hat{R}_{(i)}^{(2)}/|\hat{R}_{(i)}^{(1)}|^2]\right) + O(\epsilon^2),$$

$$\epsilon|\hat{R}_{(i)}^{(1)}|^3 K_2^{(i)} = \rho(s)c(s, \tilde{\theta})\hat{R}_{(i)}^{(1)} \cdot \hat{e}_\rho(s, \tilde{\theta}) + \epsilon\chi\partial_s[\rho(s)c(s, \tilde{\theta})]\hat{R}_{(i)}^{(1)} \cdot \hat{e}_\rho(s, \tilde{\theta})$$
$$+ \epsilon\rho(s)c(s, \tilde{\theta})\left[\hat{R}_{(i)}^{(2)} \cdot \hat{e}_\rho(s, \tilde{\theta}) - \left(\chi\kappa(s)\cos\theta_m(s, \tilde{\theta}) + \frac{d\rho(s)}{ds}\right)\hat{R}_{(i)}^{(1)} \cdot \hat{t}(s)\right.$$
$$\left. - \left(\rho(s)\kappa(s)\cos\theta_m(s, \tilde{\theta}) + \frac{3\hat{R}_{(i)}^{(1)} \cdot \hat{R}_{(i)}^{(2)}}{|\hat{R}_{(i)}^{(1)}|^2}\right)\hat{R}_{(i)}^{(1)} \cdot \hat{e}_\rho(s, \tilde{\theta})\right] + O(\epsilon^2 c). \tag{A 7}$$

A.2.2. *Simplifying the inner integrals*

From (A 6a) we have that

$$|\hat{R}_{(i)}^{(1)}| = \sqrt{\chi^2 + \gamma^2}, \tag{A 8}$$

where

$$\gamma^2 = 2\rho^2(s)[1 - \cos(\theta - \tilde{\theta})] \tag{A 9}$$

and

$$\hat{R}_{(i)}^{(1)} \cdot \hat{t}(s) = -\chi, \tag{A 10a}$$

$$\hat{R}_{(i)}^{(1)} \cdot \hat{e}_\rho(s, \tilde{\theta}) = \rho(s)[\cos(\theta - \tilde{\theta}) - 1], \tag{A 10b}$$

$$\hat{R}_{(i)}^{(2)} \cdot \hat{e}_\rho(s, \tilde{\theta}) = -\left[\frac{1}{2}\chi^2\kappa(s)\cos\theta_m(s, \tilde{\theta}) + \chi\frac{d\rho(s)}{ds}\right], \tag{A 10c}$$

where we used that $\hat{e}_\rho(s, \theta) \cdot \hat{e}_\rho(s, \tilde{\theta}) = \cos(\theta - \tilde{\theta})$.

Rewriting (A 6a), (A 6b) in the $\{\hat{\boldsymbol{t}}, \hat{\boldsymbol{n}}, \hat{\boldsymbol{b}}\}$ frame,

$$
\hat{\boldsymbol{R}}_{(i)}^{(1)} = -\chi\hat{\boldsymbol{t}}(s) + \rho(s)[\hat{\boldsymbol{e}}_\rho(s, \theta) - \hat{\boldsymbol{e}}_\rho(s, \tilde{\theta})] \tag{A 11}
$$

$$
= -\chi\hat{\boldsymbol{t}}(s) + \rho(s) \{[\cos\theta_m(s, \theta) - \cos\theta_m(s, \tilde{\theta})]\hat{\boldsymbol{n}}(s)
$$
$$
+ [\sin\theta_m(s, \theta) - \sin\theta_m(s, \tilde{\theta})]\hat{\boldsymbol{b}}(s)\}, \tag{A 12}
$$

$$
\hat{\boldsymbol{R}}_{(i)}^{(2)} = -\left[\frac{1}{2}\chi^2\kappa\hat{\boldsymbol{n}}(s) + \chi\frac{\mathrm{d}\rho(s)}{\mathrm{d}s}\hat{\boldsymbol{e}}_\rho(s, \tilde{\theta}) - \chi\rho(s)\kappa(s)\cos\theta_m(s, \tilde{\theta})\hat{\boldsymbol{t}}(s)\right] \tag{A 13}
$$

$$
= \chi\rho(s)\kappa(s)\cos\theta_m(s, \tilde{\theta})\hat{\boldsymbol{t}}(s) - \left[\frac{1}{2}\chi^2\kappa(s) + \chi\frac{\mathrm{d}\rho(s)}{\mathrm{d}s}\cos\theta_m(s, \tilde{\theta})\right]\hat{\boldsymbol{n}}(s)
$$
$$
- \chi\frac{\mathrm{d}\rho(s)}{\mathrm{d}s}\sin\theta_m(s, \tilde{\theta})\hat{\boldsymbol{b}}(s), \tag{A 14}
$$

we obtain

$$
\hat{\boldsymbol{R}}_{(i)}^{(1)} \cdot \hat{\boldsymbol{R}}_{(i)}^{(2)} = -\chi\rho(s)\left[\frac{1}{2}\kappa(s)\chi(\cos\theta_m(s, \tilde{\theta}) + \cos\theta_m(s, \theta)) + \frac{\mathrm{d}\rho(s)}{\mathrm{d}s}(\cos(\theta - \tilde{\theta}) - 1)\right]. \tag{A 15}
$$

This allows us, after some rearranging, to express the inner kernels $K_1^{(i)}$, $K_2^{(i)}$ as

$$
K_1^{(i)} = \frac{\rho(s)\mathcal{A}(s, \tilde{\theta})}{\epsilon\sqrt{\chi^2 + \gamma^2}} - \epsilon\mathcal{A}(s, \tilde{\theta})\frac{1}{\epsilon\sqrt{\chi^2 + \gamma^2}}\rho^2(s)\kappa(s)\cos\theta_m(s, \tilde{\theta})
$$
$$
+ \epsilon\rho^2(s)\mathcal{A}(s, \tilde{\theta})\left[\frac{1}{2}\frac{\kappa(s)\chi^2}{\epsilon\sqrt{\chi^2 + \gamma^2}^3}[\cos\theta_m(s, \tilde{\theta}) + \cos\theta_m(s, \theta)]\right.
$$
$$
\left.+ \frac{\chi}{\epsilon\sqrt{\chi^2 + \gamma^2}^3}\frac{\mathrm{d}\rho(s)}{\mathrm{d}s}[\cos(\theta - \tilde{\theta}) - 1]\right]
$$
$$
+ \epsilon\frac{\chi}{\epsilon\sqrt{\chi^2 + \gamma^2}}\partial_s[\rho(s)\mathcal{A}(s, \tilde{\theta})] + O(\epsilon^2), \tag{A 16}
$$

$$
K_2^{(i)} = \frac{\rho(s)c(s, \tilde{\theta})}{\epsilon\sqrt{\chi^2 + \gamma^2}^3}\rho(s)[\cos(\theta - \tilde{\theta}) - 1]
$$
$$
+ \epsilon\frac{\chi}{\epsilon\sqrt{\chi^2 + \gamma^2}^3}\rho(s)[\cos(\theta - \tilde{\theta}) - 1]\partial_s[\rho(s)c(s, \tilde{\theta})]
$$
$$
- \epsilon\frac{\rho(s)c(s, \tilde{\theta})\kappa(s)\cos\theta_m(s, \tilde{\theta})}{\epsilon\sqrt{\chi^2 + \gamma^2}^3}\left[-\frac{\chi^2}{2} + \rho^2(s)[\cos(\theta - \tilde{\theta}) - 1]\right]
$$
$$
+ 3\epsilon\frac{\rho^3(s)c(s, \tilde{\theta})}{\epsilon\sqrt{\chi^2 + \gamma^2}^5}[\cos(\theta - \tilde{\theta}) - 1]\left\{\chi\frac{\mathrm{d}\rho(s)}{\mathrm{d}s}[\cos(\theta - \tilde{\theta}) - 1]\right.
$$
$$
\left.+ \frac{\chi^2}{2}\kappa(s)[\cos\theta_m(s, \tilde{\theta}) + \cos\theta_m(s, \theta)]\right\} + O(\epsilon c/\sqrt{\chi^2 + \gamma^2}^3). \tag{A 17}
$$

Note we have deliberately not simplified ϵ in the numerators and denominators of the fractions in the above expressions and kept the fractions in the form $\chi^i/\epsilon\sqrt{\chi^2 + \gamma^2}^j$, as we will next use known expressions for their integrated values.

A.2.3. *Evaluating the inner integrals*

We can now perform the integrations with respect to $\tilde{s}$, following Koens & Lauga (2018), by using the known values of integrals of the form

$$I_j^i = \int_{-1}^1 \frac{\chi^i}{\epsilon\sqrt{\chi^2 + \gamma^2}^j}\,\mathrm{d}\tilde{s}, \tag{A 18}$$

where γ is a constant with respect to $\tilde{s}$, i,j positive integers, and we recall $\tilde{s} = s + \epsilon\chi$. The following leading-order expressions are given by Koens & Lauga (2018),

$$I_{j=1}^{i=0} = \log\left(\frac{4(1-s^2)}{\epsilon^2\gamma^2}\right), \quad I_{j=3}^{i=0} = \frac{2}{\gamma^2}, \quad I_{j=5}^{i=0} = \frac{4}{3\gamma^4}, \tag{A 19a-c}$$

$$I_{j=3}^{i=1} = \frac{2s\epsilon}{s^2-1}, \quad I_{j=5}^{i=1} = 0, \tag{A 19d,e}$$

$$I_{j=3}^{i=2} = \left[\log\left(\frac{4(1-s^2)}{\epsilon^2\gamma^2}\right) - 2\right], \quad I_{j=5}^{i=2} = \frac{2}{3\gamma^2}, \tag{A 19f,g}$$

and we also evaluate

$$\begin{aligned}
I_{j=1}^{i=1} &= \int_{-1}^1 \frac{\chi}{\epsilon\sqrt{\chi^2+\gamma^2}}\,\mathrm{d}\tilde{s} = \int_{-(1+s)/\epsilon}^{(1-s)/\epsilon} \frac{\chi}{\sqrt{\chi^2+\gamma^2}}\,\mathrm{d}\chi \\
&= \frac{1}{\epsilon}[|1-s| - |1+s|][1+O(\epsilon^2)] = -\frac{2s}{\epsilon}[1+O(\epsilon^2)],
\end{aligned} \tag{A 20}$$

where we used $|1-s| - |1+s| = (1-s) - (1+s) = -2s$ for $-1 < s < 1$. Using (A 19a) to (A 19e) in $K_1^{(i)}$, $K_2^{(i)}$ and simplifying gives

$$\begin{aligned}
\int_{-1}^1 K_1^{(i)}\,\mathrm{d}\tilde{s} &= \rho(s)\mathcal{A}(s,\tilde{\theta})\left[\log\left(\frac{2(1-s^2)}{\epsilon^2\rho^2(s)}\right) - \log[1-\cos(\theta-\tilde{\theta})]\right] \\
&\quad - 2s\partial_s[\rho(s)\mathcal{A}(s,\tilde{\theta})][1+O(\epsilon^2)] \\
&\quad - \epsilon\mathcal{A}(s,\tilde{\theta})\left[\log\left(\frac{2(1-s^2)}{\epsilon^2\rho^2(s)}\right) - \log[1-\cos(\theta-\tilde{\theta})]\right] \\
&\quad \times \rho^2(s)\kappa(s)\cos\theta_m(s,\tilde{\theta}) \\
&\quad + \epsilon\rho^2(s)\mathcal{A}(s,\tilde{\theta})\frac{1}{2}\kappa(s)[\cos\theta_m(s,\tilde{\theta}) + \cos\theta_m(s,\theta)] \\
&\quad \times \left[\log\left(\frac{2(1-s^2)}{\epsilon^2\rho^2(s)}\right) - 2 - \log[1-\cos(\theta-\tilde{\theta})]\right] \\
&\quad + \epsilon\rho^2(s)\mathcal{A}(s,\tilde{\theta})\frac{2s\epsilon}{s^2-1}\frac{\mathrm{d}\rho(s)}{\mathrm{d}s}[\cos(\theta-\tilde{\theta}) - 1] \\
&\quad + O(\epsilon^2),
\end{aligned} \tag{A 21}$$

$$\begin{aligned}
\int_{-1}^1 K_2^{(i)}\,\mathrm{d}\tilde{s} &= -c(s,\tilde{\theta}) + \frac{1}{2}\epsilon c(s,\tilde{\theta})\left[\log\left(\frac{2(1-s^2)}{\epsilon^2\rho^2(s)}\right) - \log[1-\cos(\theta-\tilde{\theta})]\right] \\
&\quad \times \kappa(s)\rho(s)\cos\theta_m(s,\tilde{\theta}) \\
&\quad - \epsilon c(s,\tilde{\theta})\frac{1}{2}\rho(s)\kappa(s)[\cos\theta_m(s,\tilde{\theta}) + \cos\theta_m(s,\theta)] \\
&\quad + \epsilon\frac{2s\epsilon}{s^2-1}\rho(s)[\cos(\theta-\tilde{\theta}) - 1]\partial_s[\rho(s)c(s,\tilde{\theta})] + O(\epsilon^2 c).
\end{aligned} \tag{A 22}$$

A.3. *Matching: common part*

In order to obtain $K_1^{(o)\in(i)}$ and $K_1^{(o)\in(i)}$, we substitute $\tilde{s} = s + \epsilon\chi$ in the expressions for $K_1^{(o)}$ and $K_2^{(o)}$ and expand. Here we show these expansions for $\boldsymbol{R}_0$, $\boldsymbol{R}_0/|\boldsymbol{R}_0|^2$ and $\mathcal{D}_{(\tilde{s},\tilde{\theta})}^{(s,\theta)}$, using the Serret–Frenet equations,

$$\boldsymbol{R}_0 = -\epsilon\chi \left[\hat{\boldsymbol{t}}(s) + \frac{1}{2}(\epsilon\chi)\kappa(s)\hat{\boldsymbol{n}}(s) \right.$$
$$\left. + \frac{(\epsilon\chi)^2}{6}[-\kappa^2(s)\hat{\boldsymbol{t}}(s) + \kappa'(s)\hat{\boldsymbol{n}}(s) + \kappa(s)\tau(s)\hat{\boldsymbol{b}}(s)] + O(\epsilon^3) \right], \qquad (A\,23a)$$

$$|\boldsymbol{R}_0| = |\epsilon\chi| \left[1 - \tfrac{1}{24}(\epsilon\chi)^2\kappa^2(s) + O(\epsilon^3) \right], \qquad (A\,23b)$$

$$\frac{\boldsymbol{R}_0}{|\boldsymbol{R}_0|^2} = -\frac{1}{(\epsilon\chi)} \left[\hat{\boldsymbol{t}}(s) + \frac{1}{2}(\epsilon\chi)\kappa(s)\hat{\boldsymbol{n}}(s) \right.$$
$$\left. + \frac{(\epsilon\chi)^2}{6}\left[-\frac{\kappa^2(s)}{2}\hat{\boldsymbol{t}}(s) + \kappa'(s)\hat{\boldsymbol{n}}(s) + \kappa(s)\tau(s)\hat{\boldsymbol{b}}(s) \right] + O(\epsilon^3) \right], \quad (A\,23c)$$

$$\mathcal{D}_{(\tilde{s},\tilde{\theta})}^{(s,\theta)} = \rho(s)[\hat{\boldsymbol{e}}_\rho(s,\theta) - \hat{\boldsymbol{e}}_\rho(s,\tilde{\theta})]$$
$$+ \epsilon\chi \left[\rho(s)\kappa(s)\cos\theta_m(s,\tilde{\theta})\hat{\boldsymbol{t}}(s) - \frac{\mathrm{d}\rho(s)}{\mathrm{d}s}\hat{\boldsymbol{e}}_\rho(s,\tilde{\theta}) \right] + O(\epsilon^2), \qquad (A\,23d)$$

$$\frac{\boldsymbol{R}_0 \cdot \mathcal{D}_{(\tilde{s},\tilde{\theta})}^{(s,\theta)}}{|\boldsymbol{R}_0|^2} = -\frac{1}{2}\rho(s)\kappa(s)[\cos\theta_m(s,\theta) + \cos\theta_m(s,\tilde{\theta})] + O(\epsilon). \qquad (A\,23e)$$

The above expansions, after some calculations lead to

$$K_1^{(o)\in(i)} = \frac{\rho(s)\mathcal{A}(s,\tilde{\theta})}{|\tilde{s} - s|} + \mathrm{sign}(\tilde{s} - s)\partial_s[\rho(s)\mathcal{A}(s,\tilde{\theta})]$$
$$- \frac{1}{2}\epsilon\frac{\rho(s)\mathcal{A}(s,\tilde{\theta})}{|\tilde{s} - s|}\rho(s)\kappa(s)[\cos\theta_m(s,\tilde{\theta}) - \cos\theta_m(s,\theta)] + O(\epsilon^2), \quad (A\,24)$$

$$K_2^{(o)\in(i)} = \epsilon^2\frac{\rho^2(s)c(s,\tilde{\theta})}{|\tilde{s} - s|^3}[\cos(\theta - \tilde{\theta}) - 1][1 + O(\epsilon)]. \qquad (A\,25)$$

Since $\int_{-1}^{1}\mathrm{sign}(\tilde{s} - s)\,\mathrm{d}\tilde{s} = \int_{-1}^{s}(-1)\,\mathrm{d}\tilde{s} + \int_{s}^{1}(+1)\,\mathrm{d}\tilde{s} = -(1 + s) + (1 - s) = -2s$ the integrals of the common parts simplify to

$$\int_{-1}^{1}\int_{-\pi}^{\pi} K_1^{(o)\in(i)}\,\mathrm{d}\tilde{s}\,\mathrm{d}\tilde{\theta} = \int_{-1}^{1}\frac{\rho(s)}{|\tilde{s} - s|}\int_{-\pi}^{\pi}\mathcal{A}(s,\tilde{\theta})\,\mathrm{d}\tilde{\theta}\,\mathrm{d}\tilde{s} + (-2s)\partial_s\int_{-\pi}^{\pi}[\rho(s)\mathcal{A}(s,\tilde{\theta})]\,\mathrm{d}\tilde{\theta}$$
$$- \frac{1}{2}\epsilon\rho^2(s)\kappa(s)\int_{-1}^{1}\frac{1}{|\tilde{s} - s|}\int_{-\pi}^{\pi}\mathcal{A}(s,\tilde{\theta})$$
$$\times [\cos\theta_m(s,\tilde{\theta}) - \cos\theta_m(s,\theta)]\,\mathrm{d}\tilde{\theta}\,\mathrm{d}\tilde{s} + O(\epsilon^2), \qquad (A\,26)$$

$$\int_{-1}^{1}\int_{-\pi}^{\pi} K_2^{(o)\in(i)}\,\mathrm{d}\tilde{s}\,\mathrm{d}\tilde{\theta} = O(\epsilon^2). \qquad (A\,27)$$

Appendix B. Expansion of the concentration field

B.1. *Full expression for the expansion of the concentration field*

The full boundary integral (BI) equations are approximated by the adding the outer and inner expansions and subtracting from each the common part,

$$
2\pi c(s, \theta) \approx \int_{-1}^{1} \int_{-\pi}^{\pi} (K_1^{(i)} + K_2^{(i)} + K_1^{(o)} + K_2^{(o)} - K_1^{(i)\in(o)} - K_2^{(i)\in(o)}) \, d\tilde{\theta} \, d\tilde{s}
$$

$$
= +\rho(s) \int_{-\pi}^{\pi} \mathcal{A}(s, \tilde{\theta}) \left[\log\left(\frac{2(1 - s^2)}{\epsilon^2 \rho^2(s)} \right) - \log[1 - \cos(\theta - \tilde{\theta})] \right] d\tilde{\theta}
$$

$$
+ (-2s) \int_{-\pi}^{\pi} \partial_s [\rho(s) \mathcal{A}(s, \tilde{\theta})] \, d\tilde{\theta} [1 + O(\epsilon^2)]
$$

$$
- \epsilon \rho^2(s) \kappa(s) \int_{-\pi}^{\pi} \mathcal{A}(s, \tilde{\theta}) \cos \theta_m(s, \tilde{\theta})
$$

$$
\times \left[\log\left(\frac{2(1 - s^2)}{\epsilon^2 \rho^2(s)} \right) - \log[1 - \cos(\theta - \tilde{\theta})] \right] d\tilde{\theta}
$$

$$
+ \frac{1}{2} \epsilon \rho^2(s) \kappa(s) \int_{-\pi}^{\pi} \mathcal{A}(s, \tilde{\theta}) [\cos \theta_m(s, \tilde{\theta}) + \cos \theta_m(s, \theta)]
$$

$$
\times \left[\log\left(\frac{2(1 - s^2)}{\epsilon^2 \rho^2(s)} \right) - 2 \right] d\tilde{\theta}
$$

$$
- \frac{1}{2} \epsilon \rho^2(s) \kappa(s) \int_{-\pi}^{\pi} \mathcal{A}(s, \tilde{\theta}) [\cos \theta_m(s, \tilde{\theta}) + \cos \theta_m(s, \theta)]
$$

$$
\times \log[1 - \cos(\theta - \tilde{\theta})] \, d\tilde{\theta}
$$

$$
+ \epsilon \rho^2(s) \frac{2s\epsilon}{s^2 - 1} \frac{d\rho(s)}{ds} \int_{-\pi}^{\pi} \mathcal{A}(s, \tilde{\theta}) [\cos(\theta - \tilde{\theta}) - 1] \, d\tilde{\theta}
$$

$$
- \int_{-\pi}^{\pi} c(s, \tilde{\theta}) d\tilde{\theta} + \frac{1}{2} \epsilon \rho(s) \kappa(s) \int_{-\pi}^{\pi} c(s, \tilde{\theta})
$$

$$
\times \left[\log\left(\frac{2(1 - s^2)}{\epsilon^2 \rho^2(s)} \right) - \log[1 - \cos(\theta - \tilde{\theta})] \right] \cos \theta_m(s, \tilde{\theta}) \, d\tilde{\theta}
$$

$$
- \frac{1}{2} \epsilon \rho(s) \kappa(s) \int_{-\pi}^{\pi} c(s, \tilde{\theta}) [\cos \theta_m(s, \tilde{\theta}) + \cos \theta_m(s, \theta)] \, d\tilde{\theta}
$$

$$
+ \epsilon \frac{2s\epsilon}{s^2 - 1} \rho(s) \int_{-\pi}^{\pi} [\cos(\theta - \tilde{\theta}) - 1] \partial_s [\rho(s) c(s, \tilde{\theta})] \, d\tilde{\theta}
$$

$$
+ \int_{-1}^{1} \frac{\rho(\tilde{s})}{|\boldsymbol{R}_0|} \int_{-\pi}^{\pi} \mathcal{A}(\tilde{s}, \tilde{\theta}) \, d\tilde{\theta} \, d\tilde{s}
$$

$$
- \epsilon \int_{-1}^{1} \frac{\rho(\tilde{s})}{|\boldsymbol{R}_0|} \int_{-\pi}^{\pi} \mathcal{A}(\tilde{s}, \tilde{\theta}) \left[\rho(\tilde{s}) \kappa(\tilde{s}) \cos \theta_m(\tilde{s}, \tilde{\theta}) + \frac{\boldsymbol{R}_0}{|\boldsymbol{R}_0|^2} \cdot \mathcal{D}_{(\tilde{s}, \tilde{\theta})}^{(s, \theta)} \right] d\tilde{\theta} \, d\tilde{s}
$$

$$
+ \epsilon \int_{-1}^{1} \frac{\rho(\tilde{s})}{|\boldsymbol{R}_0|^3} \int_{-\pi}^{\pi} c(\tilde{s}, \tilde{\theta}) \{ \boldsymbol{R}_0 \cdot \hat{\boldsymbol{e}}_\rho(\tilde{s}, \tilde{\theta}) + O(\epsilon) \} \, d\tilde{\theta} \, d\tilde{s}
$$

$$
- \int_{-1}^{1} \frac{\rho(s)}{|\tilde{s} - s|} \int_{-\pi}^{\pi} \mathcal{A}(s, \tilde{\theta}) \, \mathrm{d}\tilde{\theta} \, \mathrm{d}\tilde{s} + 2s\partial_s \int_{-\pi}^{\pi} [\rho(s)\mathcal{A}(s, \tilde{\theta})] \, \mathrm{d}\tilde{\theta}
$$

$$
+ \frac{1}{2}\epsilon\rho^2(s)\kappa(s) \int_{-1}^{1} \frac{1}{|\tilde{s} - s|} \int_{-\pi}^{\pi} \mathcal{A}(s, \tilde{\theta})
$$

$$
\times [\cos\theta_m(s, \tilde{\theta}) - \cos\theta_m(s, \theta)] \, \mathrm{d}\tilde{\theta} \, \mathrm{d}\tilde{s} + O(\epsilon^2). \tag{B 1}
$$

B.2. *Leading-order concentration field*

To leading order, after neglecting the term $\epsilon(2s\epsilon/(s^2 - 1))\rho(s) \int_{-\pi}^{\pi} [\cos(\theta - \tilde{\theta}) - 1]$ $\partial_s[\rho(s)c(s, \tilde{\theta})] \, \mathrm{d}\theta$ in the integral of $K_2^{(i)}$, equation (B 1) gives

$$
\begin{aligned}
2\pi c^{(0)}(s, \theta) + \int_{-\pi}^{\pi} c^{(0)}(s, \tilde{\theta}) \, \mathrm{d}\tilde{\theta} \approx\ & + \int_{-1}^{1} \frac{\rho(\tilde{s})}{|\boldsymbol{R}_0|} \int_{-\pi}^{\pi} \mathcal{A}(\tilde{s}, \tilde{\theta}) \, \mathrm{d}\tilde{\theta} \, \mathrm{d}\tilde{s} \\
& - \int_{-1}^{1} \frac{\rho(s)}{|\tilde{s} - s|} \int_{-\pi}^{\pi} \mathcal{A}(s, \tilde{\theta}) \, \mathrm{d}\tilde{\theta} \, \mathrm{d}\tilde{s} \\
& + \rho(s) \log\left(\frac{2(1 - s^2)}{\epsilon^2\rho^2(s)}\right) \int_{-\pi}^{\pi} \mathcal{A}(s, \tilde{\theta}) \, \mathrm{d}\tilde{\theta} \\
& - \rho(s) \int_{-\pi}^{\pi} \mathcal{A}(s, \tilde{\theta}) \log[1 - \cos(\theta - \tilde{\theta})] \, \mathrm{d}\tilde{\theta}, \tag{B 2}
\end{aligned}
$$

where the terms $\pm 2s\partial_s \int_{-\pi}^{\pi} [\rho(s)\mathcal{A}(s, \tilde{\theta})] \, \mathrm{d}\tilde{\theta}$ cancel out. Integrating this again over θ gives

$$
\begin{aligned}
4\pi \langle c^{(0)}(s) \rangle = 2\pi & \left\{ \int_{-1}^{1} \left[\frac{\rho(\tilde{s})\langle \mathcal{A}(\tilde{s}) \rangle}{|\boldsymbol{R}_0(s, \tilde{s})|} - \frac{\rho(s)\langle \mathcal{A}(s) \rangle}{|\tilde{s} - s|} \right] \mathrm{d}\tilde{s} + \rho(s)\langle \mathcal{A}(s) \rangle \log\left(\frac{2(1 - s^2)}{\epsilon^2\rho^2(s)}\right) \right\} \\
& - \rho(s) \int_{-\pi}^{\pi} \int_{-\pi}^{\pi} \mathcal{A}(s, \tilde{\theta}) \log[1 - \cos(\theta - \tilde{\theta})] \, \mathrm{d}\tilde{\theta} \, \mathrm{d}\theta, \tag{B 3} \\
= 2\pi & \left\{ \int_{-1}^{1} \left[\frac{\rho(\tilde{s})\langle \mathcal{A}(\tilde{s}) \rangle}{|\boldsymbol{R}_0(s, \tilde{s})|} - \frac{\rho(s)\langle \mathcal{A}(s) \rangle}{|\tilde{s} - s|} \right] \mathrm{d}\tilde{s} + \rho(s)\langle \mathcal{A}(s) \rangle \log\left(\frac{2(1 - s^2)}{\epsilon^2\rho^2(s)}\right) \right\} \\
& + 2\pi \log(2)\rho(s) \int_{-\pi}^{\pi} \mathcal{A}(s, \tilde{\theta}) \, \mathrm{d}\tilde{\theta}, \tag{B 4}
\end{aligned}
$$

where we simplified the last term by exchanging the order of the two integrals (over $\mathrm{d}\tilde{\theta}$ and $\mathrm{d}\theta$) and using $\int_{-\pi}^{\pi} \log[1 - \cos(\theta - \tilde{\theta})] \, \mathrm{d}\tilde{\theta} = -2\pi\log(2)$. Dividing by 2π and collecting terms we arrive at

$$
2\langle c^{(0)}(s) \rangle = + \int_{-1}^{1} \left[\frac{\rho(\tilde{s})\langle \mathcal{A}(\tilde{s}) \rangle}{|\boldsymbol{R}_0(s, \tilde{s})|} - \frac{\rho(s)\langle \mathcal{A}(s) \rangle}{|\tilde{s} - s|} \right] \mathrm{d}\tilde{s} + \rho(s)\langle \mathcal{A}(s) \rangle \log\left(\frac{4(1 - s^2)}{\epsilon^2\rho^2(s)}\right). \tag{B 5}
$$

Subtracting half of (B 5) from (B 2) we obtain the leading-order slender boundary integral equation in (2.39).

B.3. *Next-order concentration field*

Going to the next order, equation (B 1) gives the first-order correction to the slender boundary integral formula

$$
\begin{aligned}
2\pi c^{(1)}(s,\theta) = {}&-\rho^2(s)\kappa(s)\int_{-\pi}^{\pi}\mathcal{A}(s,\tilde{\theta})\cos\theta_m(s,\tilde{\theta})\\
&\times\left[\log\left(\frac{2(1-s^2)}{\epsilon^2\rho^2(s)}\right)-\log[1-\cos(\theta-\tilde{\theta})]\right]\mathrm{d}\tilde{\theta}\\
&+\frac{1}{2}\rho^2(s)\kappa(s)\int_{-\pi}^{\pi}\mathcal{A}(s,\tilde{\theta})[\cos\theta_m(s,\tilde{\theta})+\cos\theta_m(s,\theta)]\\
&\times\left[\log\left(\frac{2(1-s^2)}{\epsilon^2\rho^2(s)}\right)-2\right]\mathrm{d}\tilde{\theta}\\
&-\frac{1}{2}\rho^2(s)\kappa(s)\int_{-\pi}^{\pi}\mathcal{A}(s,\tilde{\theta})[\cos\theta_m(s,\tilde{\theta})+\cos\theta_m(s,\theta)]\\
&\times\log[1-\cos(\theta-\tilde{\theta})]\mathrm{d}\tilde{\theta}\\
&-\int_{-\pi}^{\pi}c^{(1)}(s,\tilde{\theta})\,\mathrm{d}\tilde{\theta}+\frac{1}{2}\rho(s)\kappa(s)\int_{-\pi}^{\pi}c^{(0)}(s,\tilde{\theta})\\
&\times\left[\log\left(\frac{2(1-s^2)}{\epsilon^2\rho^2(s)}\right)-\log[1-\cos(\theta-\tilde{\theta})]\right]\cos\theta_m(s,\tilde{\theta})\,\mathrm{d}\tilde{\theta}\\
&-\frac{1}{2}\rho(s)\kappa(s)\int_{-\pi}^{\pi}c^{(0)}(s,\tilde{\theta})[\cos\theta_m(s,\tilde{\theta})+\cos\theta_m(s,\theta)]\,\mathrm{d}\tilde{\theta}\\
&-\int_{-1}^{1}\frac{\rho(\tilde{s})}{|\boldsymbol{R}_0|}\int_{-\pi}^{\pi}\mathcal{A}(\tilde{s},\tilde{\theta})\\
&\times\left[\rho(\tilde{s})\kappa(\tilde{s})\cos\theta_m(\tilde{s},\tilde{\theta})+\frac{\boldsymbol{R}_0}{|\boldsymbol{R}_0|^2}\cdot\boldsymbol{\mathcal{D}}_{(\tilde{s},\tilde{\theta})}^{(s,\theta)}\right]\mathrm{d}\tilde{\theta}\,\mathrm{d}\tilde{s}+O(\epsilon^2),\\
&+\int_{-1}^{1}\frac{\rho(\tilde{s})}{|\boldsymbol{R}_0|^3}\int_{-\pi}^{\pi}c^{(0)}(\tilde{s},\tilde{\theta})\{\boldsymbol{R}_0\cdot\hat{\boldsymbol{e}}_\rho(\tilde{s},\tilde{\theta})+O(\epsilon)\}\,\mathrm{d}\tilde{\theta}\,\mathrm{d}\tilde{s}\\
&+\frac{1}{2}\rho^2(s)\kappa(s)\int_{-1}^{1}\frac{1}{|\tilde{s}-s|}\int_{-\pi}^{\pi}\mathcal{A}(s,\tilde{\theta})[\cos\theta_m(s,\tilde{\theta})-\cos\theta_m(s,\theta)]\,\mathrm{d}\tilde{\theta}\,\mathrm{d}\tilde{s}.
\end{aligned}
$$
(B 6)

In the above expression we have neglected the term $2\epsilon^2(s\rho^2(s)/(s^2-1))(\mathrm{d}\rho(s)/\mathrm{d}s)$ $\int_{-\pi}^{\pi}\mathcal{A}(s,\tilde{\theta})[\cos(\theta-\tilde{\theta})-1]\,\mathrm{d}\tilde{\theta}$ in the integral of $K_1^{(i)}$. This is permissible for prolate spheroidal ends, as the $\rho^2(s)$ in the numerator cancels the singularity in the denominator at $s=\pm1$.

For axisymmetric activity, $\mathcal{A}(s,\theta)\equiv\mathcal{A}(s)$, this simplifies as some of the integrals vanish or simplify, for example, $\int_{-\pi}^{\pi}\hat{\boldsymbol{e}}_\rho(\tilde{s},\tilde{\theta})\,\mathrm{d}\tilde{\theta}=0$ and $\int_{-\pi}^{\pi}\cos\theta_m(s,\tilde{\theta})\,\mathrm{d}\tilde{\theta}=0$,

$$
\begin{aligned}
2\pi &c^{(1)}(s,\theta)+\langle c^{(1)}(s)\rangle\\
&=+\frac{1}{2}\rho^2(s)\kappa(s)\mathcal{A}(s)\int_{-\pi}^{\pi}\cos\theta_m(s,\tilde{\theta})\log[1-\cos(\theta-\tilde{\theta})]\,\mathrm{d}\tilde{\theta}\\
&\quad+\frac{1}{2}\rho^2(s)\kappa(s)\mathcal{A}(s)\cos\theta_m(s,\theta)
\end{aligned}
$$

$$\times \left\{ 2\pi \left[\log \left(\frac{2(1-s^2)}{\epsilon^2 \rho^2(s)} \right) - 2 \right] - \int_{-\pi}^{\pi} \log[1 - \cos(\theta - \tilde{\theta})] \, d\tilde{\theta} \right\}$$

$$- \frac{1}{2} \rho(s)\kappa(s)c^{(0)}(s) \left(2\pi \cos \theta_m(s, \theta) + \int_{-\pi}^{\pi} \log[1 - \cos(\theta - \tilde{\theta})] \cos \theta_m(s, \tilde{\theta}) \, d\tilde{\theta} \right)$$

$$- 2\pi \rho(s) \int_{-1}^{1} \rho(\tilde{s})\mathcal{A}(\tilde{s}) \frac{\boldsymbol{R}_0}{|\boldsymbol{R}_0|^3} d\tilde{s} \cdot \hat{\boldsymbol{e}}_\rho(s, \theta),$$

$$- \pi \rho^2(s)\kappa(s) \int_{-1}^{1} \frac{1}{|\tilde{s} - s|} \mathcal{A}(s) \cos \theta_m(s, \theta) \, d\tilde{s}. \tag{B 7}$$

Now, as in Koens & Lauga (2018) we use that

$$\int_{-\pi}^{\pi} \log[1 - \cos(\theta - \tilde{\theta})] \, d\tilde{\theta} = -2\pi \log(2), \tag{B 8a}$$

$$\int_{-\pi}^{\pi} \log[1 - \cos(\theta - \tilde{\theta})] \cos \theta_m(s, \tilde{\theta}) \, d\tilde{\theta} = -2\pi \cos \theta_m(s, \theta), \tag{B 8b}$$

to get

$$2\pi c^{(1)}(s, \theta) + \langle c^{(1)}(s) \rangle = + \frac{1}{2} \rho^2(s)\kappa(s)\mathcal{A}(s)$$

$$\times \left(-2\pi \cos \theta_m(s, \theta) + \cos \theta_m(s, \theta) \right.$$

$$\times \left\{ 2\pi \left[\log \left(\frac{2(1-s^2)}{\epsilon^2 \rho^2(s)} \right) - 2 \right] + 2\pi \log(2) \right\} \right)$$

$$- \frac{1}{2} \rho(s)\kappa(s)c^{(0)}(s)(2\pi \cos \theta_m(s, \theta) - 2\pi \cos \theta_m(s, \theta))$$

$$- 2\pi \rho(s) \int_{-1}^{1} \rho(\tilde{s})\mathcal{A}(\tilde{s}) \frac{\boldsymbol{R}_0}{|\boldsymbol{R}_0|^3} d\tilde{s} \cdot \hat{\boldsymbol{e}}_\rho(s, \theta),$$

$$- \pi \rho^2(s)\kappa(s) \int_{-1}^{1} \frac{1}{|\tilde{s} - s|} \mathcal{A}(s) \cos \theta_m(s, \theta) \, d\tilde{s}. \tag{B 9}$$

Appendix C. Endpoint error estimation

To complement the numerical validation of our results, here we provide some analysis of the end errors in our theory. In the derivation of SPT, in particular the inner region expansion, we have assumed that $\epsilon \, d\rho/ds \ll 1$, however, for prolate spheroidal filaments $\rho(s) = \sqrt{1-s^2}$, and $d\rho/ds$ diverges close to the ends. Indeed, in the region where $\epsilon \, d\rho/ds \sim 1/\epsilon^n$, $n \geqslant 0$, we must have $s \sim 1/\sqrt{(1 + \epsilon^{2(n+1)})} \to |s| \sim 1 - \epsilon^{2(n+1)}/2$, which gives the length of the region as $\delta = O(\epsilon^{2(n+1)})$. Not accounting for this divergence at the ends introduces a small error in the concentration calculation over the filament, which we now estimate via scaling arguments on the boundary integral equation. We then discuss the slip velocity in this region, and the impact on swimming velocity.

C.1. *Error analysis for the concentration*

The concentration field over the filament is given by,

$$2\pi c(s, \theta) = \int_{-l}^{l} \int_{-\pi}^{\pi} [K_1 + K_2] \, d\tilde{\theta} \, d\tilde{s}, \tag{C 1}$$

with

$$K_1(s, \theta, \tilde{s}, \tilde{\theta}) = \frac{\mathcal{A}(\tilde{s}, \tilde{\theta})}{|\boldsymbol{R}|} \left| \frac{\partial \boldsymbol{S}}{\partial \tilde{s}} \times \frac{\partial \boldsymbol{S}}{\partial \tilde{\theta}} \right|, \quad K_2(s, \theta, \tilde{s}, \tilde{\theta}) = -\frac{c(\tilde{s}, \tilde{\theta})\boldsymbol{R}}{|\boldsymbol{R}|^3} \cdot \left(\frac{\partial \boldsymbol{S}}{\partial \tilde{s}} \times \frac{\partial \boldsymbol{S}}{\partial \tilde{\theta}} \right). \quad (C\,2)$$

Consider the expressions for the surface element and its magnitude

$$\frac{\partial \boldsymbol{S}}{\partial \tilde{s}} \times \frac{\partial \boldsymbol{S}}{\partial \tilde{\theta}} = \epsilon \rho(\tilde{s}) \left\{ \epsilon \frac{\mathrm{d}\rho(\tilde{s})}{\mathrm{d}\tilde{s}} \hat{\boldsymbol{t}}(\tilde{s}) - [1 - \epsilon \rho(\tilde{s})\kappa(\tilde{s}) \cos \theta_m(\tilde{s}, \tilde{\theta})] \hat{\boldsymbol{e}}_\rho(\tilde{s}, \tilde{\theta}) \right\}, \quad (C\,3)$$

$$\left| \frac{\partial \boldsymbol{S}}{\partial \tilde{s}} \times \frac{\partial \boldsymbol{S}}{\partial \tilde{\theta}} \right| = \epsilon \rho(\tilde{s}) \sqrt{[1 - \epsilon \rho(\tilde{s})\kappa(\tilde{s}) \cos \theta_m(\tilde{s}, \tilde{\theta})]^2 + \epsilon^2 \left(\frac{\mathrm{d}\rho(\tilde{s})}{\mathrm{d}\tilde{s}} \right)^2}. \quad (C\,4)$$

While $\mathrm{d}\rho/\mathrm{d}s$ diverges as $s \to \pm 1$, the product $\rho \, \mathrm{d}\rho/\mathrm{d}s$ remains $O(1)$. Thus, for $\epsilon \, \mathrm{d}\rho/\mathrm{d}s \sim 1$, $\rho \sim \epsilon$, and the size of the surface element $\sim \epsilon \rho \sqrt{O(1)} = O(\epsilon^2)$. Similarly, for $\epsilon \, \mathrm{d}\rho/\mathrm{d}s \gg 1$, the size of the surface element $\sim \epsilon \rho \sqrt{(\epsilon \, \mathrm{d}\rho/\mathrm{d}s)^2} \sim \epsilon^2 \rho \, \mathrm{d}\rho/\mathrm{d}s = O(\epsilon^2)$.

Following the argument of Koens & Lauga (2018), in the inner expansion, $|\boldsymbol{R}| = O(\epsilon)$, hence in the region δ near the ends, scaling (C 2) gives $K_1 \sim (1/\epsilon)\epsilon^2 = O(\epsilon)$, $K_2 \sim (c\epsilon/\epsilon^3)\epsilon^2 = O(1)$, since $c = O(1)$. Thus, returning to the boundary integral equation, the error in the integral from either endpoint c_{err},

$$c_{err} \sim \int_{-l}^{-l+\delta} \int_{-\pi}^{\pi} K_1 + K_2 \, \mathrm{d}\tilde{\theta} \, \mathrm{d}\tilde{s} \sim (\epsilon + 1)\delta \sim \delta. \quad (C\,5)$$

Thus at worst, the contribution to the concentration along the filament from the end regions is region is $O(\epsilon^2)$, and therefore negligible.

C.2. *The slip velocity*

The slip velocity is given by (2.3). Using (C 3) and (C 4), we evaluate the normal to the filament's surface, pointing out of the filament, as

$$\boldsymbol{n}_f(s, \theta) = \frac{[1 - \epsilon \rho(s)\kappa(s) \cos \theta_m(s, \theta)] \hat{\boldsymbol{e}}_\rho(s, \theta) - \epsilon \dfrac{\mathrm{d}\rho(s)}{\mathrm{d}s} \hat{\boldsymbol{t}}(s)}{\sqrt{[1 - \epsilon \rho(s)\kappa(s) \cos \theta_m(s, \theta)]^2 + \epsilon^2 \left(\dfrac{\mathrm{d}\rho(s)}{\mathrm{d}s} \right)^2}}. \quad (C\,6)$$

The boundary condition of (2.2) allows us to write the slip velocity as

$$\begin{aligned} \boldsymbol{v}_{slip}|_S &= \mathcal{M}(\boldsymbol{x})(\boldsymbol{1} - \boldsymbol{n}_f \boldsymbol{n}_f) \cdot \nabla c \\ &= \mathcal{M}(\nabla c + \boldsymbol{n}_f \mathcal{A}), \end{aligned} \quad (C\,7)$$

and using the local cylindrical polars (with the axisymmetry axis along $\hat{\boldsymbol{t}}(s)$), we have that

$$\nabla c = \hat{\boldsymbol{t}}(\hat{\boldsymbol{t}} \cdot \nabla c) + \hat{\boldsymbol{e}}_\theta(\hat{\boldsymbol{e}}_\theta \cdot \nabla c) + \hat{\boldsymbol{e}}_\rho(\hat{\boldsymbol{e}}_\rho \cdot \nabla c), \quad (C\,8)$$

$$= \hat{\boldsymbol{t}} \partial_s c + \hat{\boldsymbol{e}}_\theta \frac{1}{\epsilon \rho} \partial_\theta c + \hat{\boldsymbol{e}}_\rho(\hat{\boldsymbol{e}}_\rho \cdot \nabla c), \quad (C\,9)$$

where in the last line we used that $\hat{\boldsymbol{t}} \cdot \nabla c = \partial_s c$, $\hat{\boldsymbol{e}}_\theta \cdot \nabla c = (1/\epsilon\rho(s))\partial_\theta c$. Using the boundary condition in (2.2) ($\boldsymbol{n}_f \cdot \nabla c = -\mathcal{A}$), together with the expression for $\boldsymbol{n}_f$ in (C 6), we can evaluate $\hat{\boldsymbol{e}}_\rho \cdot \nabla c$ as

$$(\hat{\boldsymbol{e}}_\rho \cdot \nabla c) = \frac{1}{[1 - \epsilon\rho\kappa\cos\theta_m]} \left\{ \epsilon \frac{\mathrm{d}\rho(s)}{\mathrm{d}s}\partial_s c - \mathcal{A}\sqrt{[1 - \epsilon\rho\kappa\cos\theta_m]^2 + \epsilon^2\left(\frac{\mathrm{d}\rho(s)}{\mathrm{d}s}\right)^2} \right\}.$$

(C 10)

Thus we calculate the slip velocity by substituting in the expressions for ∇c (equation (C 9)) and $\boldsymbol{n}_f$ (equation (C 6)) in (C 10)

$$\frac{1}{\mathcal{M}}\boldsymbol{v}_{slip} = \hat{\boldsymbol{t}}\partial_s c + \hat{\boldsymbol{e}}_\theta \frac{1}{\epsilon\rho}\partial_\theta c + \hat{\boldsymbol{e}}_\rho(\hat{\boldsymbol{e}}_\rho \cdot \nabla c) + \boldsymbol{n}_f \mathcal{A}$$

$$= \hat{\boldsymbol{t}}\partial_s c + \hat{\boldsymbol{e}}_\theta \frac{1}{\epsilon\rho}\partial_\theta c + \hat{\boldsymbol{e}}_\rho \frac{\epsilon\dfrac{\mathrm{d}\rho(s)}{\mathrm{d}s}\partial_s c - \mathcal{A}\sqrt{[1 - \epsilon\rho\kappa\cos\theta_m]^2 + \epsilon^2\left(\dfrac{\mathrm{d}\rho(s)}{\mathrm{d}s}\right)^2}}{[1 - \epsilon\rho\kappa\cos\theta_m]}$$

$$+ \frac{[1 - \epsilon\rho\kappa\cos\theta_m(s, \theta)]\hat{\boldsymbol{e}}_\rho - \epsilon\dfrac{\mathrm{d}\rho(s)}{\mathrm{d}s}\hat{\boldsymbol{t}}}{\sqrt{[1 - \epsilon\rho\kappa\cos\theta_m(s, \theta)]^2 + \epsilon^2\left(\dfrac{\mathrm{d}\rho(s)}{\mathrm{d}s}\right)^2}}\mathcal{A}.$$

(C 11)

C.3. *Swimming velocity error analysis*

We now proceed to estimate the effect of the regions with large variations in the cross-sectional radius $\rho(s)$ in the swimming velocity. We focus our attention on the prolate spheroidal cross-sectional profile $\rho(s) = \sqrt{1 - s^2}$ and show that in both regions (see the following §§ C.3.1 and C.3.2), the contribution of the endpoint region to the swimming kinematics is negligible at leading order.

Note the form of the normal vector to the filament surface close to the endpoints,

$$\epsilon\frac{\mathrm{d}\rho(s)}{\mathrm{d}s} = O(1), \quad \text{then} \quad \boldsymbol{n}_f(s, \theta) = \frac{\hat{\boldsymbol{e}}_\rho(s, \theta) - \epsilon\dfrac{\mathrm{d}\rho(s)}{\mathrm{d}s}\hat{\boldsymbol{t}}(s)}{\sqrt{1 + \epsilon^2\left(\dfrac{\mathrm{d}\rho(s)}{\mathrm{d}s}\right)^2}} + O(\epsilon), \quad \text{(C 12a)}$$

$$\epsilon\frac{\mathrm{d}\rho(s)}{\mathrm{d}s} = O(1/\epsilon^n), \quad n \geqslant 1, \quad \text{then} \quad \boldsymbol{n}_f(s, \theta) = -\mathrm{sign}\left(\epsilon\frac{\mathrm{d}\rho(s)}{\mathrm{d}s}\right)\hat{\boldsymbol{t}} + O(\epsilon^n). \quad \text{(C 12b)}$$

At $s = \pm 1$, $\boldsymbol{n}_f = \pm\hat{\boldsymbol{t}}$, and the boundary condition for the flux gives us that $\partial_s c = \pm\mathcal{A}(s = \pm 1)$. Since in the majority of the filament $s \in (-1 + \epsilon^2, 1 - \epsilon^2)$ we have $\partial_s c = O(1)$ (provided one is away from a jump in activity), by continuity we therefore expect $\partial_s c = O(1)$ in the region δ. Similarly, we will assume that, provided activity is axisymmetric in the region δ, we have $\partial_\theta c = O(\epsilon\rho)$.

Since we are interested in the contribution of the end regions to the swimming kinematics, we estimate $\int_{-\pi}^{\pi}\int_{1-|s|=O(\delta)}\boldsymbol{v}_{slip}(s, \theta)\,\mathrm{d}\theta\,\mathrm{d}s$ where δ is the arclength extend of the region close to the endpoints in each of the cases examined below. For the purposes of the scaling analysis, we assume $\mathcal{M} = 1$.

C.3.1. *Region with $\epsilon(\mathrm{d}\rho(s)/\mathrm{d}s) = O(1)$*

For $\rho(s) = \sqrt{1 - s^2}$ this region has size $\delta = O(\epsilon^2)$ and within it $\rho = O(\epsilon)$. We can estimate the scalings of the various terms in the surface slip velocity as follows:

$$\int_{-\pi}^{\pi} \int_{1-|s|=O(\delta)} \boldsymbol{v}_{slip}(s, \theta)\, \mathrm{d}\theta\, \mathrm{d}s$$

$$= \underbrace{\int_{-\pi}^{\pi} \int_{1-|s|=O(\delta)} \hat{\boldsymbol{t}}(s)(\partial_s c)}_{O(\delta \cdot 1)=O(\epsilon^2)} + \underbrace{\int_{-\pi}^{\pi} \int_{1-|s|=O(\delta)} \hat{\boldsymbol{e}}_\theta \frac{1}{\epsilon\rho}(\partial_\theta c)}_{O(\delta \cdot 1/\epsilon^2 \cdot \epsilon^2)=O(\epsilon^2) \text{ for axisymm } \mathcal{A}}$$

$$+ \underbrace{\int_{-\pi}^{\pi} \int_{1-|s|=O(\delta)} \hat{\boldsymbol{e}}_\rho \epsilon \frac{\mathrm{d}\rho(s)}{\mathrm{d}s}(\partial_s c)[1 + O(\epsilon^2)]}_{O(\delta \cdot 1)=O(\epsilon^2)}$$

$$- \underbrace{\int_{-\pi}^{\pi} \int_{1-|s|=O(\delta)} \hat{\boldsymbol{e}}_\rho \mathcal{A}\sqrt{1 + \epsilon^2\left(\frac{\mathrm{d}\rho(s)}{\mathrm{d}s}\right)^2}[1 + O(\epsilon^2)]}_{O(\delta \cdot 1)=O(\epsilon^2)}$$

$$+ \underbrace{\int_{-\pi}^{\pi} \int_{1-|s|=O(\delta)} \mathcal{A}\frac{\hat{\boldsymbol{e}}_\rho - \epsilon\dfrac{\mathrm{d}\rho(s)}{\mathrm{d}s}\hat{\boldsymbol{t}}}{\sqrt{1 + \epsilon^2\left(\dfrac{\mathrm{d}\rho(s)}{\mathrm{d}s}\right)^2}}[1 + O(\epsilon^2)]}_{O(\delta \cdot 1)=O(\epsilon^2)}. \tag{C 13}$$

Thus, the regions of size $O(\epsilon^2)$, in which $\epsilon(\mathrm{d}\rho(s)/\mathrm{d}s) = O(1)$, make an $O(\epsilon^2)$ contribution to the swimming kinematics, which is negligible compared with the leading-order swimming kinematics.

C.3.2. *Region with $\epsilon(\mathrm{d}\rho(s)/\mathrm{d}s) \sim 1/\epsilon^n$, $n \geqslant 1$*

For $\rho(s) = \sqrt{1 - s^2}$, the region in which $\epsilon(\mathrm{d}\rho(s)/\mathrm{d}s) \sim 1/\epsilon^n$, $n \geqslant 1$ has size $\delta = O(\epsilon^{2n+2})$, within it $\rho = O(\epsilon^{n+1})$, and hence we can estimate the scalings of the various terms in the surface slip velocity as follows:

$$\int_{-\pi}^{\pi} \int_{1-|s|=O(\delta)} \boldsymbol{v}_{slip}(s, \theta)$$

$$= \underbrace{\int_{-\pi}^{\pi} \int_{1-|s|=O(\delta)} \hat{\boldsymbol{t}}(s)(\partial_s c)}_{O(\delta \cdot 1)=O(\epsilon^{2n+2})} + \underbrace{\int_{-\pi}^{\pi} \int_{1-|s|=O(\delta)} \hat{\boldsymbol{e}}_\theta \frac{1}{\epsilon\rho}(\partial_\theta c)}_{O(\delta \cdot 1)=O(\epsilon^{2n+2})}$$

$$+ \underbrace{\int_{-\pi}^{\pi} \int_{1-|s|=O(\delta)} \hat{\boldsymbol{e}}_\rho \epsilon \frac{\mathrm{d}\rho(s)}{\mathrm{d}s}(\partial_s c)}_{O(\delta(1/\epsilon^n)\cdot 1)=O(\epsilon^{n+2})} - \underbrace{\int_{-\pi}^{\pi} \int_{1-|s|=O(\delta)} \hat{\boldsymbol{e}}_\rho \mathcal{A}\left|\epsilon \frac{\mathrm{d}\rho(s)}{\mathrm{d}s}\right|}_{O(\delta(1/\epsilon^n))=O(\epsilon^{n+2})}$$

$$+ \underbrace{\int_{-\pi}^{\pi} \int_{1-|s|=O(\delta)} -\mathcal{A}\,\mathrm{sign}\left(\epsilon \frac{\mathrm{d}\rho(s)}{\mathrm{d}s}\right)\hat{\boldsymbol{t}} + O(\epsilon^n)}_{O(\delta \cdot 1)=O(\epsilon^{2n+2})}. \tag{C 14}$$

Thus, the regions of size $O(\epsilon^{2n+2})$ in which $\epsilon(\mathrm{d}\rho(s)/\mathrm{d}s) = O(1/\epsilon^n)$, make an $O(\epsilon^{n+2})$ contribution to the swimming kinematics, which is negligible compared to the leading-order swimming kinematics.

REFERENCES

ANDERSON, J. L. 1989 Colloid transport by interfacial forces. *Annu. Rev. Fluid Mech.* **21** (1), 61–99.

BAKER, R. D., MONTENEGRO-JOHNSON, T. D., SEDIAKO, A. D., THOMSON, M. J., SEN, A., LAUGA, E. & ARANSON, I. S. 2019 Shape-programmed 3D printed swimming microtori for the transport of passive and active agents. *Nat. Commun.* **10** (1), 1–10.

BERTIN, N., SPELMAN, T. A., STEPHAN, O., GREDY, L., BOURIAU, M., LAUGA, E. & MARMOTTANT, P. 2015 Propulsion of bubble-based acoustic microswimmers. *Phys. Rev.* A **4** (6), 064012.

BLAKE, J. R. 1971 Self propulsion due to oscillations on the surface of a cylinder at low Reynolds number. *Bull. Austral. Math. Soc.* **5** (2), 255–264.

BROWN, A. & POON, W. 2014 Ionic effects in self-propelled Pt-coated Janus swimmers. *Soft Matt.* **10**, 4016–4027.

CHWANG, A. T. & WU, T. Y.-T. 1975 Hydromechanics of low-Reynolds-number flow. Part 2. Singularity method for Stokes flows. *J. Fluid Mech.* **67** (4), 787–815.

COX, R. G. 1970 The motion of long slender bodies in a viscous fluid. Part 1. General theory. *J. Fluid Mech.* **44** (4), 791–810.

DREYFUS, R., BAUDRY, J., ROPER, M. L., FERMIGIER, M., STONE, H. A. & BIBETTE, J. 2005 Microscopic artificial swimmers. *Nature* **437** (7060), 862–865.

EBBENS, S., GREGORY, D. A., DUNDERDALE, G., HOWSE, J. R., IBRAHIM, Y., LIVERPOOL, T. B. & GOLESTANIAN, R. 2014 Electrokinetic effects in catalytic platinum-insulator Janus swimmers. *Eur. Phys. Lett.* **106**, 58003.

GAFFNEY, E. A., GADÊLHA, H., SMITH, D. J., BLAKE, J. R. & KIRKMAN-BROWN, J. C. 2011 Mammalian sperm motility: observation and theory. *Annu. Rev. Fluid Mech.* **43**, 501–528.

GAO, W., SATTAYASAMITSATHIT, S., MANESH, K. M., WEIHS, D. & WANG, J. 2010 Magnetically powered flexible metal nanowire motors. *J. Am. Chem. Soc.* **132** (41), 14403–14405.

GHOSH, A. & FISCHER, P. 2009 Controlled propulsion of artificial magnetic nanostructured propellers. *Nano Lett.* **9** (6), 2243–2245.

GOLESTANIAN, R., LIVERPOOL, T. B. & AJDARI, A. 2007 Designing phoretic micro- and nano-swimmers. *New J. Phys.* **9** (5), 126.

GÖTZ, T. 2000 Interactions of fibers and flow: asymptotics, theory and numerics. PhD thesis, University of Kaiserslautern, Germany.

GRAY, J. & HANCOCK, G. J. 1955 The propulsion of sea-urchin spermatozoa. *J. Expl Biol.* **32** (4), 802–814.

HALL-MCNAIR, A. L., MONTENEGRO-JOHNSON, T. D., GADÊLHA, H., SMITH, D. J. & GALLAGHER, M. T. 2019 Efficient implementation of elastohydrodynamics via integral operators. *Phys. Rev. Fluids* **4** (11), 113101.

HANCOCK, G. J. 1953 The self-propulsion of microscopic organisms through liquids. *Proc. R. Soc. Lond.* A **217** (1128), 96–121.

HAPPEL, J. & BRENNER, H. 1965 *Low Reynolds Number Hydrodynamics*. Prentice Hall.

HOWSE, J. R., JONES, R. A. L., RYAN, A. J., GOUGH, T., VAFABAKHSH, R. & GOLESTANIAN, R. 2007 Self-motile colloidal particles: from directed propulsion to random walk. *Phys. Rev. Lett.* **99**, 048102.

IBRAHIM, Y., GOLESTANIAN, R. & LIVERPOOL, T. 2017 Shape dependent phoretic propulsion of slender active particles. *Phys. Rev. Fluids* **3** (3), 033101.

JOHNSON, R. E. 1979 An improved slender-body theory for Stokes flow. *J. Fluid Mech.* **99**, 411–431.

KOENS, L. & LAUGA, E. 2018 The boundary integral formulation of Stokes flows includes slender-body theory. *J. Fluid Mech.* **850**, R1.

LAMB, H. 1932 *Hydrodynamics*, 6th edn. Dover.

LAUGA, E. & POWERS, T. R. 2009 The hydrodynamics of swimming microorganisms. *Rep. Prog. Phys.* **72** (9), 096601.

MAGGI, C., SIMMCHEN, J., SAGLIMBENI, F., KATURI, J., DIPALO, M., DE ANGELIS, F., SANCHEZ, S. & DI LEONARDO, R. 2016 Self-assembly of micromachining systems powered by Janus micromotors. *Small* **12** (4), 446–451.

MICHELIN, S. & LAUGA, E. 2014 Phoretic self-propulsion at finite Péclet numbers. *J. Fluid Mech.* **747**, 572–604.

MICHELIN, S. & LAUGA, E. 2017 Geometric tuning of self-propulsion for Janus catalytic particles. *Sci. Rep.* **7**, 42264.

MONTENEGRO-JOHNSON, T. D., MICHELIN, S. & LAUGA, E. 2015 A regularised singularity approach to phoretic problems. *Eur. Phys. J.* E **38** (12), 1–7.

MONTENEGRO-JOHNSON, T. D. 2018 Microtransformers: controlled microscale navigation with flexible robots. *Phys. Rev. Fluids* **3**, 062201.

MOREAU, C., GIRALDI, L. & GADÊLHA, H. 2018 The asymptotic coarse-graining formulation of slender-rods, bio-filaments and flagella. *J. R. Soc. Interface* **15** (144), 20180235.

NELSON, B. J., KALIAKATSOS, I. K. & ABBOTT, J. J. 2010 Microrobots for minimally invasive medicine. *Annu. Rev. Biomed. Engng* **12**, 55–85.

PAXTON, W. F., KISTLER, K. C., OLMEDA, C. C., SEN, A., ANGELO, S. K. S., CAO, Y., MALLOUK, T. E., LAMMERT, P. E. & CRESPI, V. H. 2004 Catalytic nanomotors: autonomous movement of striped nanorods. *J. Am. Chem. Soc.* **126** (41), 13424–13431.

POZRIKIDIS, C. 1992 *Boundary Integral and Singularity Methods for Linearized Viscous Flow*. Cambridge University Press.

SCHNITZER, O. & YARIV, E. 2015 Osmotic self-propulsion of slender particles. *Phys. Fluids* **27** (3), 031701.

SCHOELLER, S. F., TOWNSEND, A. K., WESTWOOD, T. A. & KEAVENY, E. E. 2019 Methods for suspensions of passive and active filaments. arXiv:1903.12609.

SMITH, D. J., GAFFNEY, E. A. & BLAKE, J. R. 2008 Modelling mucociliary clearance. *Respir. Physiol. Neurobiol.* **163** (1–3), 178–188.

SMITH, D. J., MONTENEGRO-JOHNSON, T. D. & LOPES, S. S. 2019 Symmetry-breaking cilia-driven flow in embryogenesis. *Annu. Rev. Fluid Mech.* **51**, 105–128.

SPAGNOLIE, S. E. & LAUGA, E. 2011 Comparative hydrodynamics of bacterial polymorphism. *Phys. Rev. Lett.* **106** (5), 058103.

VARMA, A., MONTENEGRO-JOHNSON, T. D. & MICHELIN, S. 2018 Clustering-induced self-propulsion of isotropic autophoretic particles. *Soft Matt.* **14** (35), 7155–7173.

WALKER, B. J., ISHIMOTO, K., GADÊLHA, H. & GAFFNEY, E. A. 2019 Filament mechanics in a half-space via regularised stokeslet segments. *J. Fluid Mech.* **879**, 808–833.

WILLIAMS, B. J., ANAND, S. V., RAJAGOPALAN, J. & SAIF, M. T. A. 2014 A self-propelled biohybrid swimmer at low Reynolds number. *Nat. Commun.* **5**, 3081.

YARIV, E. 2008 Slender-body approximations for electro-phoresis and electro-rotation of polarizable particles. *J. Fluid Mech.* **613**, 85–94.

YARIV, E. 2019 Self-diffusiophoresis of slender catalytic colloids. *Langmuir*.

ZHANG, L., ABBOTT, J. J., DONG, L., KRATOCHVIL, B. E., BELL, D. & NELSON, B. J. 2009*a* Artificial bacterial flagella: fabrication and magnetic control. *Appl. Phys. Lett.* **94**, 064107.

ZHANG, L., ABBOTT, J. J., DONG, L., PEYER, K. E., KRATOCHVIL, B. E., ZHANG, H., BERGELES, C. & NELSON, B. J. 2009*b* Characterizing the swimming properties of artificial bacterial flagella. *Nano Lett.* **9**, 3663–3667.